JCB Journal of Cell Biology

ARTICLE

ATM is activated by ATP depletion and modulates mitochondrial function through NRF1

Hei-Man Chow[1,2], Aifang Cheng[1], Xuan Song[1], Mavis R. Swerdel[3], Ronald P. Hart[3], and Karl Herrup[1]

Ataxia-telangiectasia (A-T) is an autosomal recessive disease caused by mutation of the *ATM* gene and is characterized by loss of cerebellar Purkinje cells, neurons with high physiological activity and dynamic ATP demands. Here, we show that depletion of ATP generates reactive oxygen species that activate ATM. We find that when ATM is activated by oxidative stress, but not by DNA damage, ATM phosphorylates NRF1. This leads to NRF1 dimerization, nuclear translocation, and the up-regulation of nuclear-encoded mitochondrial genes, thus enhancing the capacity of the electron transport chain (ETC) and restoring mitochondrial function. In cells lacking ATM, cells replenish ATP poorly following surges in energy demand, and chronic ATP insufficiency endangers cell survival. We propose that in the absence of ATM, cerebellar Purkinje cells cannot respond adequately to the increase in energy demands of neuronal activity. Our findings identify ATM as a guardian of mitochondrial output, as well as genomic integrity, and suggest that alternative fuel sources may ameliorate A-T disease symptoms.

Introduction

Mitochondrial diseases commonly involve neurological symptoms, and ataxia resulting from cerebellar atrophy and Purkinje cell loss is the most frequent of these (Bargiela et al., 2015). In one cohort study of 345 patients afflicted with a range of different mitochondrial diseases, 225 (65%) showed symptoms of ataxia (Lax et al., 2012; Bargiela et al., 2015). The reverse relationship is also found (Bargiela et al., 2015): of persons showing symptoms of definitive ataxia, one-fifth also present with features of mitochondrial dysfunction. Thus, ataxia is linked to mitochondrial defects and vice versa (Scheibye-Knudsen et al., 2013; Fang et al., 2014). This bidirectional correlation led us to consider the protein involved in the inherited ataxia known as ataxia-telangiectasia (A-T), a debilitating autosomal recessive multisystem disease caused by a mutation of the *ATM* gene (Watters, 2003). The protein product of the *ATM* gene was originally identified as a large PI3K-kinase family member that functions as a DNA damage response protein. While various mechanisms have been proposed to explain the cerebellar focus of A-T neuropathology, the links between the loss of ATM function and the selective susceptibility of cerebellar neurons to neurodegeneration remain largely unknown.

ATP regulation is critical for a nerve cell. A typical resting neuron contains a billion ATP molecules, yet the firing of only a single action potential is estimated to require the hydrolysis of 10–100 million ATPs to fully restore the resting membrane potential (Howarth et al., 2010, 2012). This estimate underscores the dynamic nature of the ATP supply in neurons and raises questions as to how the levels of such a critical molecule are regulated. Thus, neuronal health and survival are heavily dependent on the constant availability of adequate supplies of ATP. The predominant site of ATP production is the mitochondrion, through the reactions of the TCA cycle and the oxidative phosphorylation (OXPHOS) reactions of the electron transport chain (ETC; Hall et al., 2012). The five complexes of the ETC are assembled from the protein products of hundreds of genes, most of which are encoded by the nuclear genome (DiMauro and Rustin, 2009). The highly deleterious effects of mutations in these genes demonstrate that even minor structural changes in ETC proteins disrupt electron transport and ATP production and can thus cause a range of conditions recognized as mitochondrial diseases that usually have profound impacts on brain functioning.

We report here that a previously unrecognized relationship exists between ATM and the regulation of ATP production in the neuronal mitochondrion. ATM deficiency results in compromised activities of the TCA cycle and ETC, leading to a reduced capacity to respond to increases in ATP demand. This newly discovered activity of ATM is mediated through nuclear respiratory factor-1 (NRF1). We propose that in the absence of ATM, neurons, in particular mature cerebellar Purkinje cells, cannot respond adequately to the increased in energy demands from neuronal

[1]Division of Life Science and The State Key Laboratory of Molecular Neuroscience, Hong Kong University of Science and Technology, Hong Kong; [2]Institute for Advanced Study, Hong Kong University of Science and Technology, Hong Kong; [3]Department of Cell Biology and Neuroscience, Rutgers University, New Brunswick, NJ.

Correspondence to Karl Herrup: herrup@ust.hk; Hei-Man Chow: heimanchow@ust.hk.

https://doi.org/10.1083/jcb.201806197

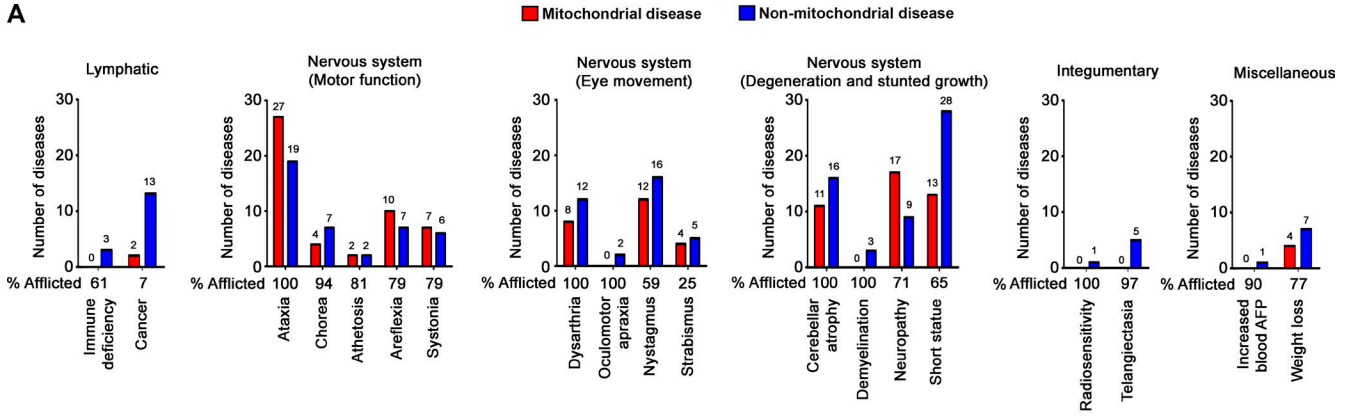

B

	Mitochondrial disease	Defective gene(s)	Mitochondrial function defect
1	MERRF	Multiple MT-genes	Multiple defects in respiratory chains enzyme activities
2	NARP	*MTATP6*	H(+)-ATPase
3	Co-Q10 deficiency	*COQ10D1±COQ2*	Compromised complex I-III and complex II-III activities
4	IOSCA	*C10orf2*	Deficiency of complexes I and IV
5	SDHA deficiency	*SDHA*	Deficiency of complex II
6	MTDPS11	*MGME1*	Multiple defects in respiratory chain enzyme activities
7	SCA28	*AFG3L2*	Multiple defects in respiratory chain enzyme activities
8	SPG7	*SPG7*	Deficiency of complex IV
9	LBSL	*DARS2*	N/A

Figure 1. **The neurological symptoms from A-T associated with mitochondrial diseases. (A)** The number of mitochondrial and nonmitochondrial diseases whose symptoms map to individual clinical symptoms of A-T, determined using MitoDB. The percentages of A-T patients associated with each symptom are listed at the bottom. **(B)** A list of common mitochondrial diseases associated with symptoms of ataxia and cerebellar atrophy.

activity. The resulting ATP deficit leads to their degeneration and the observed ataxia and other neurological deficits of A-T.

Results

ATM-related deficits in the respiratory chain and TCA cycle

As predicted from the observed correlation between mitochondrial diseases and cerebellar ataxia (Lax et al., 2012; Bargiela et al., 2015), symptoms of A-T cluster with those typically found in diseases involving the mitochondrion (Scheibye-Knudsen et al., 2013; Fang et al., 2014). To confirm this in an unbiased manner, we used the MitoDB web application to screen all reported A-T clinical symptoms for their association with mitochondrial function. Peripheral symptoms failed to show any meaningful mitochondrial association, but central nervous system phenotypes, such as cerebellar atrophy and ataxia, showed a strong overlap (Fig. 1, A and B; and Table S1 A), indicating a connection between ATM and mitochondrial function that is most prominent in the nervous system. With this in mind, we reanalyzed earlier microarray results (Li et al., 2013) from human A-T and control cerebellar cortex. Of >31,000 transcripts analyzed, 23% showed significant changes in A-T (Fig. 2 A and Table S1, B and C). The altered transcripts fell most prominently into 30 Gene Ontology (GO) groups ($P < 0.0001$; Fig. 2 B and Table S1 D; Chang and Nevins, 2006). Enrichment clustering based on the total number of genes associated with a GO term (Fig. 2 C) identified several primary metabolic pathways. Using gene set enrichment analysis (GSEA), we further identified 73 Kyoto Encyclopedia of Genes and Genomes (KEGG) pathways with nominal $P < 0.01$ (Table S1 E). Pathways associated with OXPHOS (Fig. 2 D) and the TCA cycle (Fig. 2 E) were significantly depleted in A-T (adjusted $P < 0.05$). We therefore performed subanalyses on 1,158 genes encoding mitochondria-localized proteins as indicated in the MitoCarta 2.0 inventory (Calvo et al., 2016). Expression of 458 (41%) of the nuclear-encoded, mitochondrial genes was significantly altered in A-T samples (Fig. 2 F and Table S1 F). Among these, 83% had reduced expression ($P < 0.05$), many of which associated with mitochondrial functions (Fig. 2 G and Table S1 G). This predicts a generalized loss of nuclear-encoded mitochondrial proteins in A-T and suggests that ATM function is crucial to sustain their presence.

Reduced expression and function of metabolic enzymes is associated with lack of ATM

Given the conserved nature of most mitochondrial proteins, we sought validation in the *Atm*$^{-/-}$ mouse model. Biogenesis of a functional OXPHOS system requires not only the core structural proteins of Complexes I–V, it also requires an array of OXP HOS assembly factors, as well as proteins needed for cofactor biogenesis (Fig. 3 A and Table S1 H; Koopman et al., 2013). In the *Atm*$^{-/-}$ mouse cerebellum, as in the A-T human samples (Fig. S1 A), expression of genes encoding proteins constituting these critical components was significantly reduced (Fig. S1, B–F). A notable exception to this downward trend was the increased expression of genes for proteins involved in mitochondrial DNA repair and maintenance of the mitochondrial deoxynucleotide pool (Fig. S1 F and Table S1 H), suggesting that the cells were mounting a sustained response to enhanced mitochondrial DNA damage. Furthermore, chronic inhibition of ATM activity in cell culture led to similar observations (Fig. 3, B–F). At the functional level, we analyzed the activities of Complexes I–IV in cultured *Atm*$^{-/-}$ cortical neurons, which were all significantly impaired (Fig. 3 G–J, left). The F_1F_0-ATP synthase (Complex V) trended lower, although not significantly (Fig. 3 K, left). Importantly, total

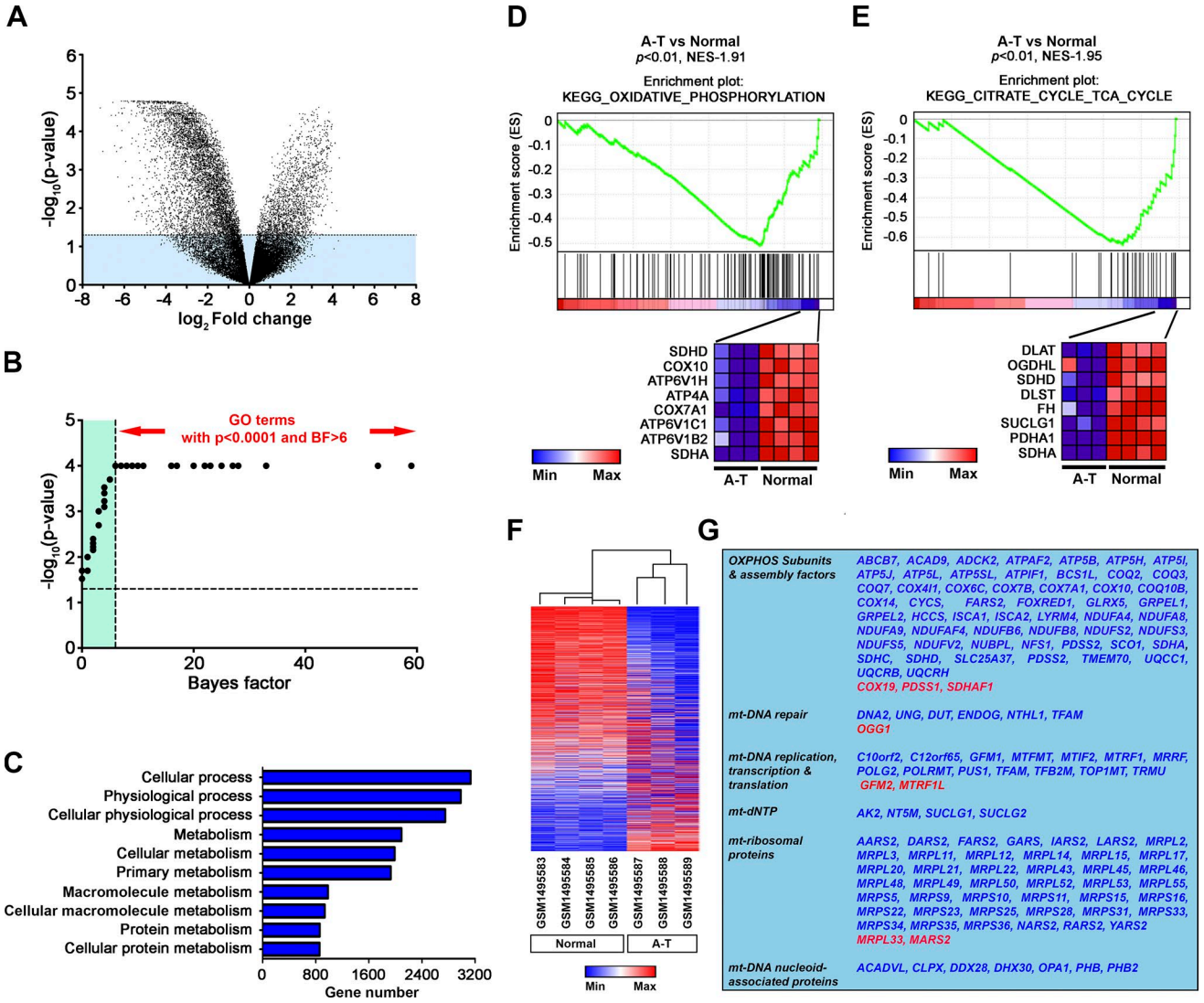

Figure 2. **Loss of metabolic function in mitochondria of A-T patients. (A)** Volcano plot of differentially expressed genes in cerebellar samples of A-T patients (n = 3) versus age-matched controls (n = 4). Genes with significant differences in expression (adjusted P < 0.05) are in the white area above the dotted line. **(B and C)** GO analysis of differentially expressed genes (Table S1 D). 30 GO terms with P < 0.0001 were plotted against the corresponding BFs (B). Enrichment ranking of pathways with significance metrics above the recommended threshold (P < 0.0001 and BF > 6) was performed (C). Pathways significantly enriched, determined by the relative number of genes associated within a GO category. **(D and E)** GSEA of significantly different genes; among significant differences were pathways of OXPHOS (D) and the TCA cycle (E). Genes with the highest enrichment score are shown as a gene expression–based heat map. **(F)** Heat map summarizing 1,116 nuclear genes encoding proteins with a high likelihood of mitochondrial localization segregated by function. **(G)** Significantly changed genes were mostly diminished in A-T (blue gene names). Gene names marked in red are relatively up-regulated. Note: 42 genes from the original MitoCarta2.0 list failed to match probes from the human expression array.

mitochondrial DNA content was unchanged in *Atm*$^{-/-}$ neurons (Fig. S1 G), implying that the effects seen in the mitochondria are due to a defect in nuclear gene expression rather than mitochondrial number. Similar observations were found in WT neurons with inhibited ATM activity (Fig. 3, G–K, right). Together, these point to the conclusion that the A-T neurological phenotype has deep roots in neuronal energy metabolism.

Altered metabolic dependence of ATM-deficient cells

Previous studies indicated that TCA cycle metabolites are altered in the cerebellum of *Atm*$^{-/-}$ mice (Fang et al., 2016). By reevaluating our published human cerebellar microarray data (Fig. 4 A), we found that the gene expression of hexokinase-1/2 (*HK1/2*), the first rate-limiting enzyme of glycolysis, was significantly reduced in A-T. This suggested that glycolysis might be diminished, and indeed, levels of the end product pyruvate were significantly reduced in cultured A-T human fibroblasts (Fig. 4 B). Treatment of WT human fibroblasts with 2-deoxyglucose (2-DG), a hexokinase inhibitor (Chen and Guéron, 1992), diminished pyruvate levels in WT cells to those seen in A-T fibroblasts (Fig. 4 B). Pyruvate can either enter mitochondria and be converted to acetyl-CoA by pyruvate dehydrogenase (PDHA1) or remain in the cytoplasm where it is converted to lactate by lactate dehydrogenase (LDH; McCommis and Finck, 2015). Since the gene expression array data showed that *LDH* was increased but *PDHA1* was dramatically reduced in *Atm*$^{-/-}$ cells (Fig. 4 A), it appears that pyruvate

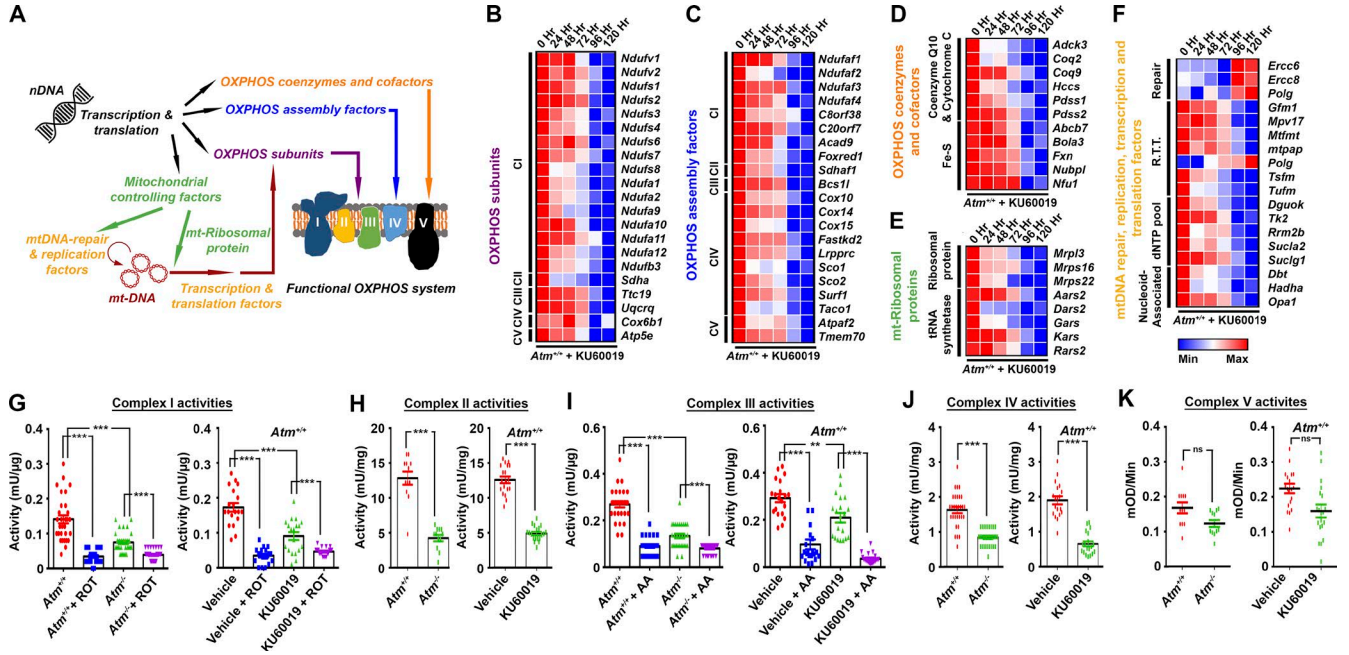

Figure 3. **Loss of *Atm* impairs the function of OXPHOS complexes in mouse neurons. (A)** Diagram indicating the assembly of the functional OXPHOS system. **(B–F)** Heat maps indicating the expression of 79 nuclear-encoded genes, whose loss of function results in neurodegeneration in cultured DIV 14 primary cortical neurons from WT mice treated with 1 µM KU60019 for the times indicated (CI–CV labels indicate genes associated with Complexes I–V). **(G–K)** Activity of each mitochondrial complex of mouse cortical neurons was measured by colorimetric assays. Left: WT versus *Atm*$^{-/-}$. Right: Vehicle or 1 µM KU60019 for 96 h (Complexes I and III–V: *n* = 30; Complex II: *n* = 12; ***, P < 0.001; ns, nonsignificant; unpaired *t* test).

is both reduced and steered toward the production of lactate in the cytoplasm. Further supporting this hypothesis, UK5099, an inhibitor of the mitochondrial pyruvate carrier (MPC; Hildyard et al., 2005), resulted in an ∼50% elevation of pyruvate levels in WT cells, but no significant change in A-T cells (Fig. 4 B). Treatment with the LDH inhibitor oxamate (Novoa et al., 1959) elevated pyruvate levels in A-T cells, while having no significant effect on WT cells (Fig. 4 B). Regarding lactate, p-chloromercuribenzene sulfonate (pCMBS) treatment, which inhibits lactate efflux from the cell, increased lactate inside A-T cells, but had no effect on WT cells. In contrast, blocking lactate production with oxamate returned lactate in A-T cells to normal levels, but had no effect on WT cells. Mouse primary neurons isolated from *Atm*$^{-/-}$ mice (Fig. S2 A) and WT neurons silenced by *Atm*-specific siRNA (Fig. S2 B) both gave similar observations (Fig. S2, C–F). Thus, in A-T cells mitochondrial pyruvate is lost while cytosolic lactate is increased.

Once pyruvate enters the mitochondrion it enters the TCA cycle. We noticed genes for subsequent steps of the TCA cycle before the formation of succinate remained unchanged, but reactions downstream from succinate were significantly reduced in A-T (Fig. 4 A). Consistent with these array results, colorimetric assays revealed that the levels of mitochondrial isocitrate were reduced by more than two-thirds (Fig. 4 D), while a near-doubling of mitochondrial succinate levels was found in A-T cells (Fig. 4 E). This situation in A-T cells would seem to be energetically precarious. We therefore considered alternative carbon sources, such as fatty acid and ketone body catabolism, which enter the TCA cycle through carnitine palmitoyltransferase (CPT). Unfortunately, the mitochondrial isoform of *CPT* (*CPT2*) is reduced by two-thirds in A-T cells (Fig. 4 A). Earlier findings from our laboratory showed that dietary supplements of the amino acid glutamine in *Atm*$^{-/-}$ mice alleviated their symptoms and extended their lifespan (Chen et al., 2016a). As the mitochondrial *GLS* isoform *GLS2* was increased fivefold in A-T cells (Fig. 4 A), it appears possible that A-T cells use glutamine as their source of carbon for the TCA cycle, as was also confirmed by the Mito Fuel Flex test (Fig. 4 E).

ATM-deficient cells have an impaired response to enhanced energy demand

We next investigated how the observed abnormalities affected overall mitochondrial function in ATM-deficient cells. Using tetramethylrhodamine methylester (TMRM) fluorescence to assess mitochondrial membrane potential (Δψm), steady-state signals in *Atm*$^{-/-}$ neurons were 1.4-fold higher than in WT controls (Fig. 5 A). In examining the cellular response to stress, however, an opposite relationship was observed. Oligomycin, an inhibitor of the F_1F_0-ATP synthase, caused a rapid reduction in Δψm in *Atm*$^{-/-}$ cells, but a slow, sustained increase in WT, presumably because in the presence of oligomycin, protons were no longer used to power the ATP synthase (Fig. 5 B). Results were similar in human A-T fibroblasts (Fig. S3, A and B), which could be a result of impaired OXPHOS Complex V that favors ATP hydrolysis to drive the proton pump and sustain Δψm (McKenzie et al., 2007; Abramov et al., 2010). These observations suggest ATM-deficient cells are less flexible in adapting to changes in energy demand. To validate this, we measured the dynamic changes in mitochondrial oxygen consumption rate (OCR). Basal OCR in mouse *Atm*$^{-/-}$ neurons (Fig. 5 D) and human A-T fibroblasts (Fig. S3 D) was not

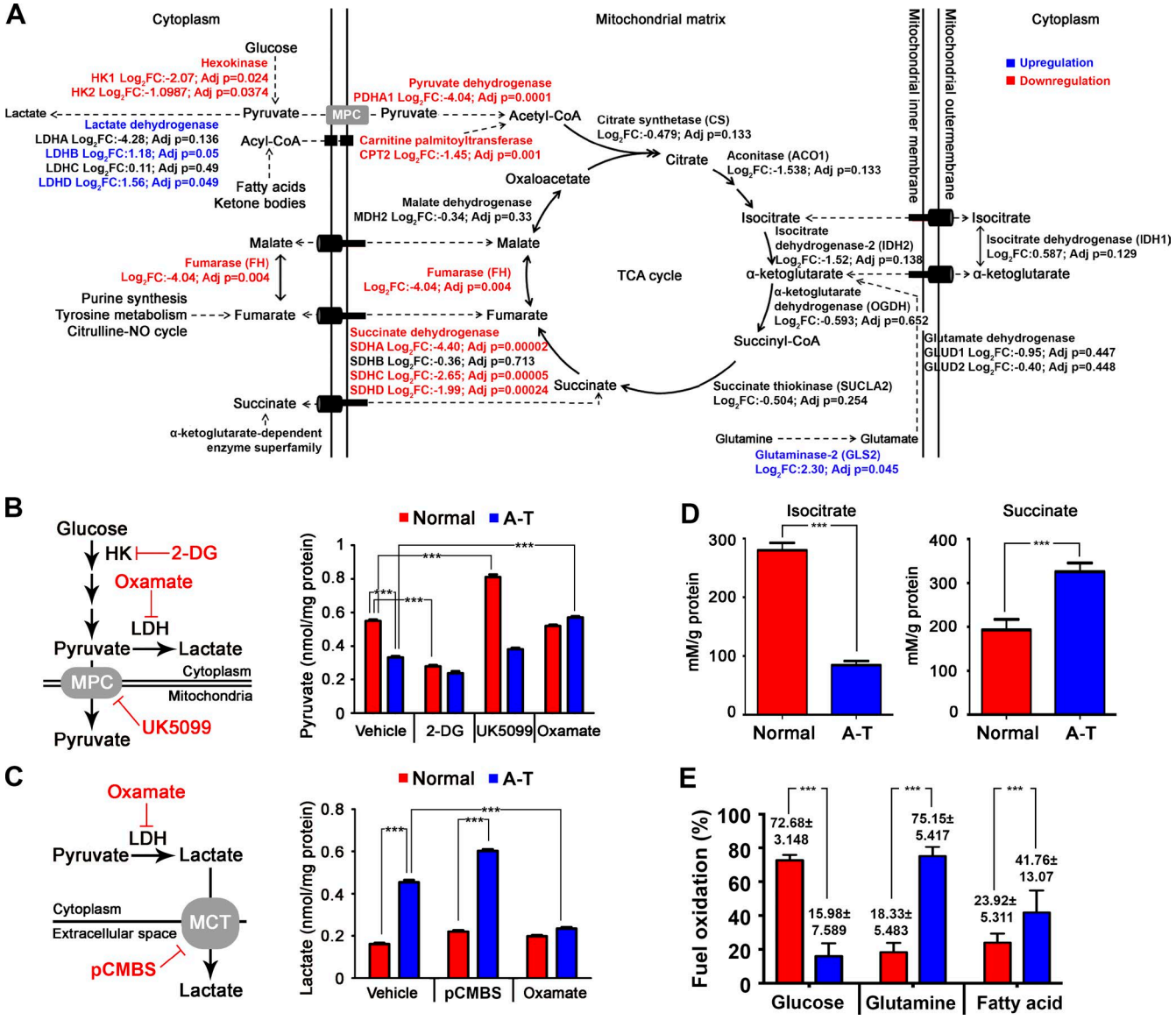

Figure 4. **Loss of *Atm* impairs the TCA cycle and favors the conversion of pyruvate to lactate over acetyl-CoA. (A)** Diagram of the TCA cycle. Enzymes up-regulated in A-T are shown in blue; down-regulated enzymes are shown in red (adjusted P ≤ 0.05). Those with no significant change are in black. **(B and C)** The levels of pyruvate (B) and lactate (C) measured by colorimetric assays under different treatment conditions (n = 18; ***, P < 0.001; one-way ANOVA). **(D)** Levels of mitochondrial isocitrate and succinate in A-T human fibroblast were determined by colorimetric assays (n = 18; ***, P < 0.001; ns, non-significant, unpaired t test). **(E)** Seahorse Mito Fuel Flex test to evaluate cellular respiration in human fibroblast under conditions when specific metabolic pathways (glucose, glutamine, or fatty acids) were inhibited. The relative fuel dependence was calculated (n = 3; ***, P < 0.001; ns, nonsignificant; unpaired t test).

significantly different from controls. The drop in OCR after treatment with oligomycin reveals the oxygen consumed by the ATP synthase was nearly identical among the cells (Fig. 5 D and Fig. S3 D). This demonstrates that under resting conditions, the respiratory activity of both WT and ATM-deficient cells are similar. However, subsequent treatment of the cells with carbonyl cyanide 4-(trifluoromethoxy)phenylhydrazone (FCCP) which drives maximal OCR revealed that ATM-deficient cells had a reduced response, which implies that the reserve respiratory capacity is significantly smaller (Fig. 5 D and Fig S3 D, dashed lines). These together suggest that less ATP is available in response to surges in neuronal energy demand. Indeed, under equilibrium conditions, the levels of ATP were reduced by one quarter in mouse *Atm*$^{-/-}$ cortical neurons (Fig. 5 E) and by nearly one half in A-T human fibroblasts (Fig. S3 E). We synaptically activated the cultured neurons for 30 s with glutamate to produce large fluxes of sodium and potassium and thus stimulate the accelerated hydrolysis of ATP by the Na^+/K^+-pump. We then monitored the ATP/ADP ratio in real time using the PercevalHR biosensor (Tantama et al., 2013). In WT cultures, glutamate treatment resulted in a rapid 50% reduction in the ATP/ADP ratio, but over the next 30 min, the ratio returned to prestimulus levels (Fig. 5, F and G). In *Atm*$^{-/-}$ cultures, while the initial reduction in the ATP/ADP ratio was nearly the same as in controls, the rate of recovery was significantly slower (Fig. 5, F and G). Emphasizing this point further, while WT cells could recover fully after glutamate, the

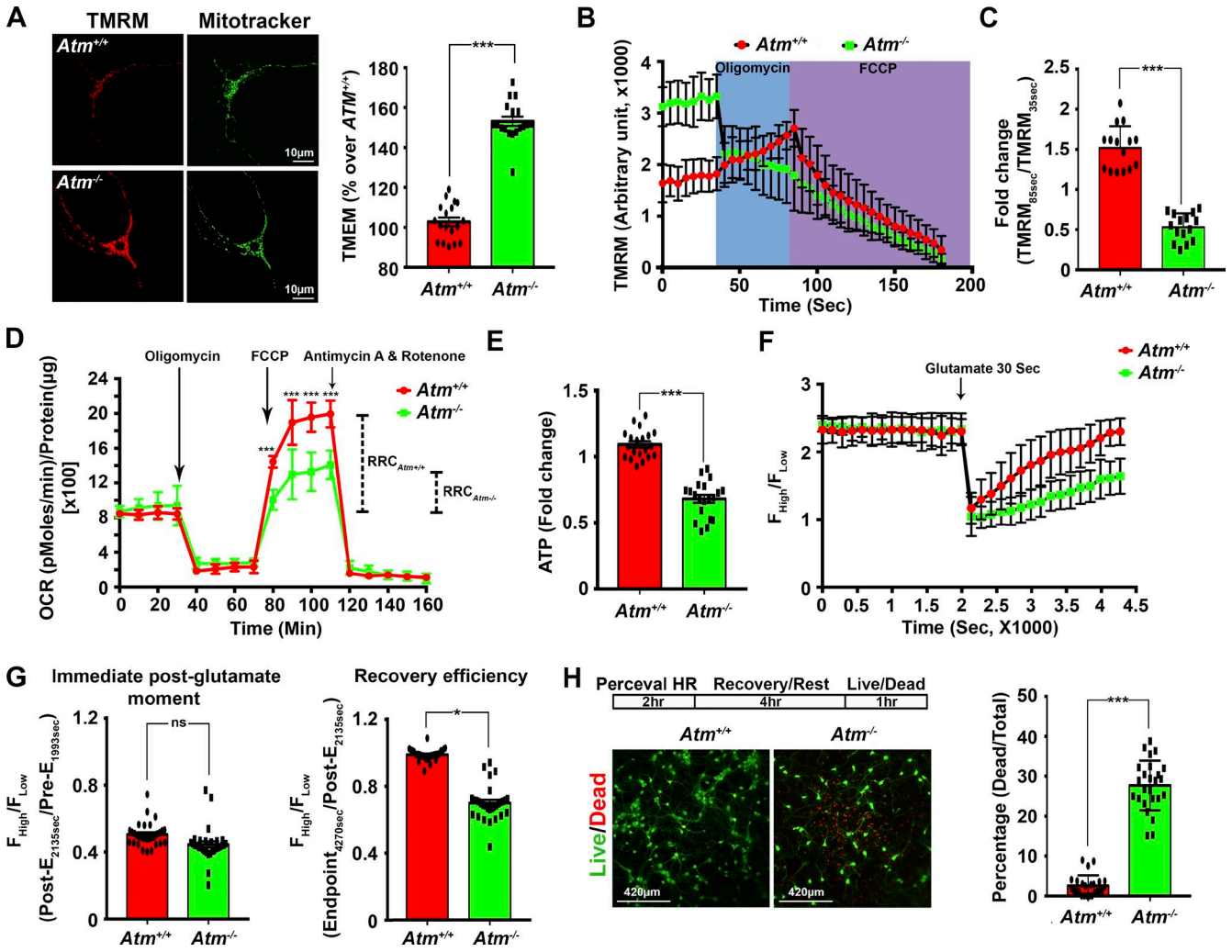

Figure 5. **Loss of *Atm* impairs cellular response toward ATP insufficiency in neurons. (A and B)** Static (A) and dynamic (B) measurements of mitochondrial membrane potential using TMRM and counterstained with Mitotracker Green (n = 15; ***, P < 0.001; unpaired t test). **(C)** The relative changes in TMRM signals, expressed as the ratio of OCR values postoligomycin (85 s) signal over preoligomycin (35 s; n = 15; ***, P < 0.001; unpaired t test). **(D)** Seahorse Mito Stress assay in primary cortical neurons (n = 16; ***, P < 0.001; two-way ANOVA). **(E and F)** Static and dynamic changes (F) in neuronal ATP levels measured by the Perceval HR reporter. **(E)** Equilibrium ATP levels at the instant before the dynamic experiment (n = 20; ***, P < 0.001; unpaired t test). **(F)** Live-imaging of cultured neuron responses to synaptic activity–dependent energy consumption. After establishing a steady baseline, 50 μM glutamate was added for 30 s (arrow) to excite the neurons and cause ATP to be consumed; glutamate was then washed away, and intracellular ATP levels were allowed to recover (n = 30; ***, P < 0.001; two-way ANOVA). **(G)** The relative abundance of ATP immediately following the removal of glutamate (Signal ratio: Post-$E_{2,135s}$/Pre-$E_{1,993sec}$; left) and after recovery (Signal ratio: Endpoint$_{4,270sec}$/Post-$E_{2,135sec}$; right; n = 30; *, P < 0.05; ns, nonsignificant; unpaired t test). **(H)** Representative images of the LIVE/DEAD status of neurons 4 h after Perceval HR assay. (Live cell: green; dead cell: red.) Quantification shown, right (n = 25; ***, P < 0.001; unpaired t test).

treatment killed nearly a quarter of the *Atm*$^{-/-}$ cells (Fig. 5 H). These data show that cells lacking ATM are unable to respond to increased energy demands and are thus more vulnerable during periods of high activity.

NRF1 links ATM activity and mitochondrial function

To determine how ATM deficiency led to the observed defects in ATP generation, we analyzed all transcript isoforms of genes that were differentially expressed in A-T and control samples as revealed in array data (12,931 transcripts from 7,222 genes). ATM itself is a serine/threonine kinase with no known DNA-binding capacity; if it were to modulate gene expression, it would most likely work through modulating activities of one or more transcription factors. We therefore searched promoter regions (−450 to +50 bp) of all differentially regulated transcripts for potential transcription factor–binding sequences using PSCAN (Zambelli et al., 2009), which identified 71 transcription factors that were significantly associated with the differentially expressed genes (Table S1 J). Of these 71, NRF1 ranked highest (Fig. 6 A). Among the 12,931 transcripts, binding sequences with >85% similarity to the NRF1 consensus motif were found in about one-third of them (4,624 promoters belonging to 3,360 genes; Fig. 6, B and C). NRF1 is a basic leucine zipper (bZIP) transcription factor that functions principally as a transactivator of nuclear-encoded respiratory genes (Evans and Scarpulla, 1990; Scarpulla, 2008). With its emergence as a strong candidate to explain the ATM-mediated changes in ATP, we analyzed expression patterns of the 3,360 genes identified as potentially regulated by

NRF1 (Table S1 K). >80% of these were significantly reduced in A-T cerebellar samples (Fig. 6 D and Table S1 L). Furthermore, of 2,470 NRF1 targets identified in both the ENCODE database and a previous NRF1 chromatin immunoprecipitation sequencing study (Satoh et al., 2013), 440 appeared in our list of genes with altered expression in A-T (Fig. 6 E). KEGG pathway analysis of these genes identified cell cycle, Wnt signaling, OXPHOS, and circadian rhythm pathways as significantly affected (Fig. 6 F). We next used immunohistochemistry to determine the anatomical location of NRF1 protein in normal and ATM-deficient brain. In WT mouse and control human samples, NRF1 immunoreactivity was substantially enriched in Purkinje cells compared with other cerebellar cell types. In the absence of ATM, NRF1 immunostaining in Purkinje cells was reduced and this reduction was most dramatic in the cell nucleus (Fig. 6 G). The implication of these findings is that ATM regulates NRF1 levels as well as its nuclear-cytoplasmic shuttling.

ATP depletion activates ATM with downstream effects on NRF1

Several studies have shown that ATM can function as a redox sensor because it can be activated by oxidative stress independently of its response to DNA damage (Guo et al., 2010; Ashley et al., 2012). We wondered, therefore, whether transient reductions in ATP might lead to ETC imbalances and that the resulting increase in ROS might activate ATM. To test this, we induced a modest depletion of ATP by treating cells with atractyloside (an inhibitor of the ADP/ATP carrier) or a more dramatic ATP depletion with oligomycin. Oligomycin resulted in significant cell death due to the severe ATP depletion (Fig. S4, A and B), yet neither atractyloside nor oligomycin induced a significant DNA damage response (Fig. 7 A). Confident that our results would not be confounded by an independent response of ATM to DNA damage, we used the less toxic atractyloside to test primary cultures of mouse neurons. We observed a good correlation between the atractyloside-induced oxidative stress and its progressive depletion of ATP (Fig. S4 C). To determine whether this ATP depletion-induced oxidative stress could activate ATM and impact NRF1, we tracked the subcellular location of NRF1 and activated (phosphorylated) ATM. Oxidative damage induced either directly with hydrogen peroxide (H_2O_2) or indirectly with atractyloside resulted in nuclear localization of both phospho-ATM and NRF1 (Fig. 7, B and C). Significantly, the actions of both drugs were blocked by the anti-oxidant, N-acetyl cysteine (NAC; Fig. 7, B and C). We determined that ATM was required for this response as NRF1 nuclear localization in response to either H_2O_2 or atractyloside was lost in *Atm*$^{-/-}$ neurons (Fig. 7, B and C). Equally important, induction of DNA damage alone was insufficient to trigger the NRF1 response. Etoposide, a topoisomerase II inhibitor that leads to DNA double strand breaks (Fig. 7 A), failed to reduce ATP levels (Fig. S4 A) or stimulate the translocation of NRF1 to the nucleus (Fig. 7, B and C).

NRF1 helps to coordinate the expression of nuclear and mitochondrial genomes. We therefore suspected that nuclear localization of NRF1 was predictive of its transcriptional activity. Using the NRF1mitoGFP reporter, which contains NRF1-binding sequences driving GFP protein expression fused with a mitochondrial localization signal, allowed us to simultaneously monitor NRF1-mediated transcriptional activity, as well as mitochondrial morphology (Hodneland Nilsson et al., 2015). As predicted from the NRF1 nuclear localization, we observed that moderate but chronic depletion of ATP induced NRF1-mediated transcription (Fig. 7 D and Fig. S4 D). In contrast, when ATM activity was lost, or with NAC cotreatment, induction of NRF1 activity was abolished (Fig. 7 D and Fig. S4 D). Significantly, in the presence of ATM, the mitochondria appeared to maintain their normal filamentous morphologies while in ATM-deficient situations, the mitochondria appeared more fragmented (Fig. S4 E). Thus, in conditions when cellular ATP is chronically in demand, ATM is required to stimulate NRF1 activity and up-regulate mitochondrial capacities. These results suggest that the oxidative activation of ATM induced by suboptimal cellular ATP levels results in nuclear localization of NRF1 with important consequences for nuclear encoded mitochondrial gene expression.

We next asked how the kinase activity of ATM was able to alter the transcriptional activity of NRF1. NRF1 binds to its DNA recognition site as a homodimer whose formation is triggered by phosphorylation of the monomer (Gugneja and Scarpulla, 1997). While *NRF1* gene transcription levels were not significantly different (Fig. 8 A), Western blots revealed that in ATM-deficient cells, the level of NRF1 protein was reduced, and the fraction of total NRF1 that was present as a dimer dropped significantly (Fig. 8 B). Scrutiny of the NRF1 protein sequences of four mammalian species identified a total of eight well-conserved (S/T)Q sequences, canonical ATM target sites (Fig. 8 C). To determine whether these sites were ATM-targeted, we coexpressed FLAG-tagged WT ATM and GFP-tagged NRF1 in *Atm*$^{-/-}$ in mouse embryonic fibroblasts (MEFs). Subsequent immunoprecipitation revealed a robust physical interaction between the two proteins (Fig. 8 D). Furthermore, Western blots of the immunoprecipitates probed with a phospho(S/T)Q antibody revealed a strong band that was missing if a kinase-dead (KD) FLAG-ATM construct was used instead of a WT one (Fig. 8 E). (S/T)Q phosphorylation of NRF1 was also lost in cultures treated with an ATM inhibitor (1 µM KU60019) but not with inhibitors of A-T and Rad 3–related (ATR; 0.5 µM VE821) or DNA-PK (20 nM NU7441; Fig. 8 F). These data suggest that specific ATM phosphorylation facilitates the homodimerization of NRF1. Although there are a total of eight potential (S/T)Q phosphorylation sites on NRF1 (Fig. 8 C), only the T259 residue located within the DNA-binding and dimerization domain (DIM) was previously identified by mass spectroscopy (Hornbeck et al., 2015) as a likely site for the dimerization site. In our search for the relevant ATM target we therefore focused on T259 and created mutant clones of the NRF1 protein (Fig. 8 G). In the presence of WT ATM, coexpression of the WT NRF1 protein or the NLS-deletion mutant (NLSdel) resulted in robust phosphorylation of the (S/T)Q site (Fig. 8 G). However, when the deletion was extended into the DNA-binding and DIM (DIMdel: T87-E283), the (S/T)Q phosphorylation signal was lost (Fig. 8 G). Refining the ATM target residue still further, expression clones that carried threonine-to-alanine triple (T201A, T259A, and T287A), double (T201A and T259A) mutations, or the single (T259A) mutation resulted in similar loss of (S/T)Q phosphorylation (Fig. 8 G), indicating these residues are potential ATM targets. Testing single

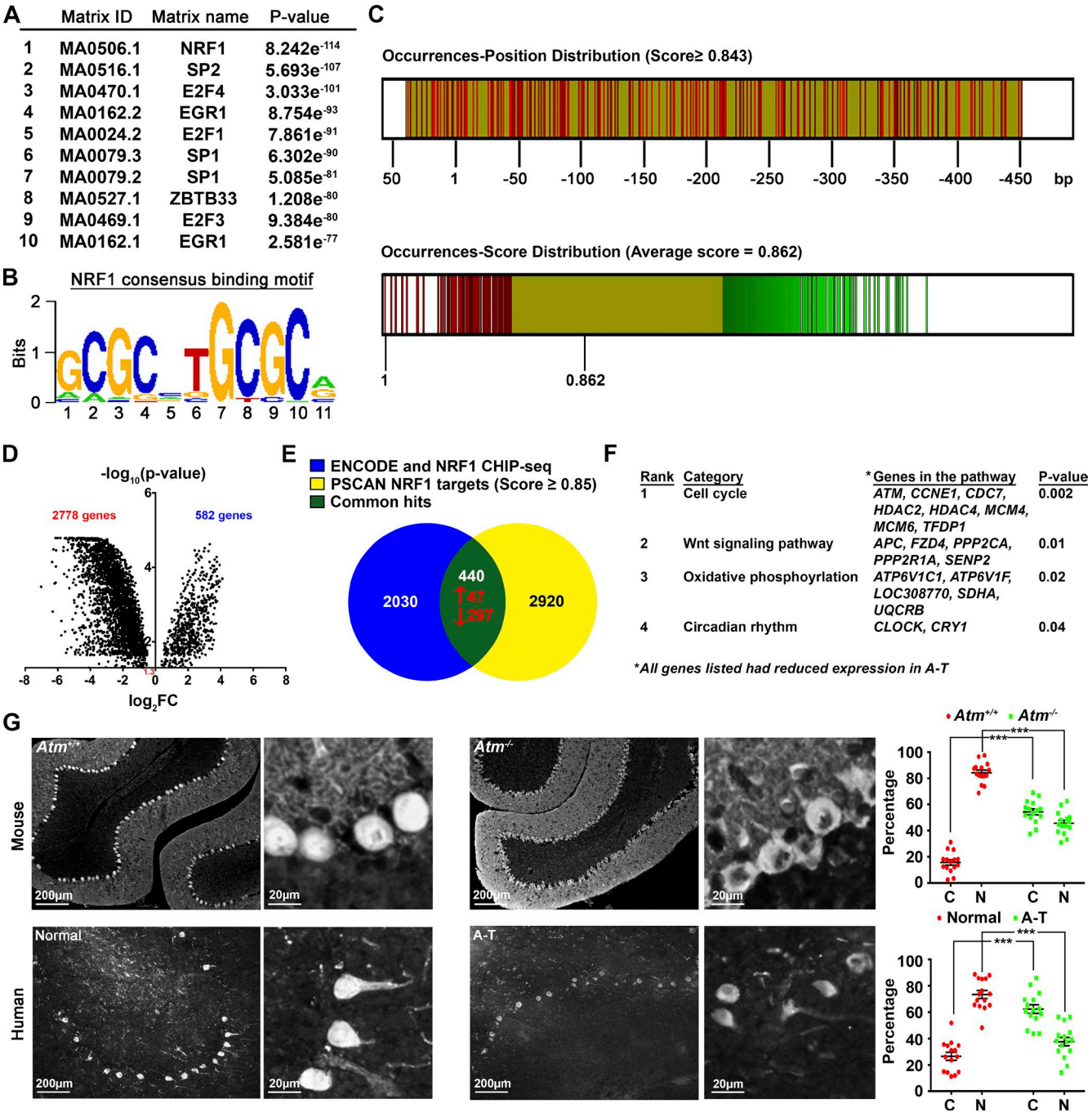

Figure 6. **NRF1 links ATM activity and mitochondrial function. (A)** The top 10 over-represented transcription factors predicted by the PSCAN platform, ranked according to their z-test P value. **(B)** The consensus sequence for these NRF1 binding sites. **(C)** Top shows the location of the best-predicted NRF1-binding motifs within the −450 to +50 bp region on the tested promoters with corresponding matching scores (the value representing the likelihood for NRF1 to bind to the promoter), higher than the average genome-wide matching score 0.843. Bottom shows the distribution scores for tested promoters, with an average matching score values of all predictions equaling 0.862, higher than the average genome-wide matching score 0.843. These, together with the z-test P value shown in A, imply that the NRF1-binding motif is nonrandomly enriched in the tested set of promoters, in which the gene expression level was significantly altered in A-T cerebella samples. Predictions on each promoter were colored as straight lines according to their corresponding matching score (red, high; yellow, medium; and green, low). **(D)** Volcano plot showing the P value of the relative expression levels of the genes predicted to be regulated by NRF1. **(E)** Venn diagram illustrating the overlap between the set of genes computationally identified as NRF1 targets (yellow) and the combined sets of observed NRF1 targets found in the ENCODE database and a published NRF1-chromatin immunoprecipitation sequencing study (blue). **(F)** A table showing the four KEGG pathways identified using genes whose promoters scored as one of the 400 top hits for likelihood as an NRF1 promoter. Genes associated in the pathways as well as the corresponding P values are shown. **(G)** Representative images of NRF1 immunostaining in mouse (top) and human (bottom) cerebellar tissue samples. Quantification of Purkinje cells with cytoplasmic (C) and nuclear (N) NRF1 in cells are shown on the right (n = 15; ***, P < 0.001; one-way ANOVA).

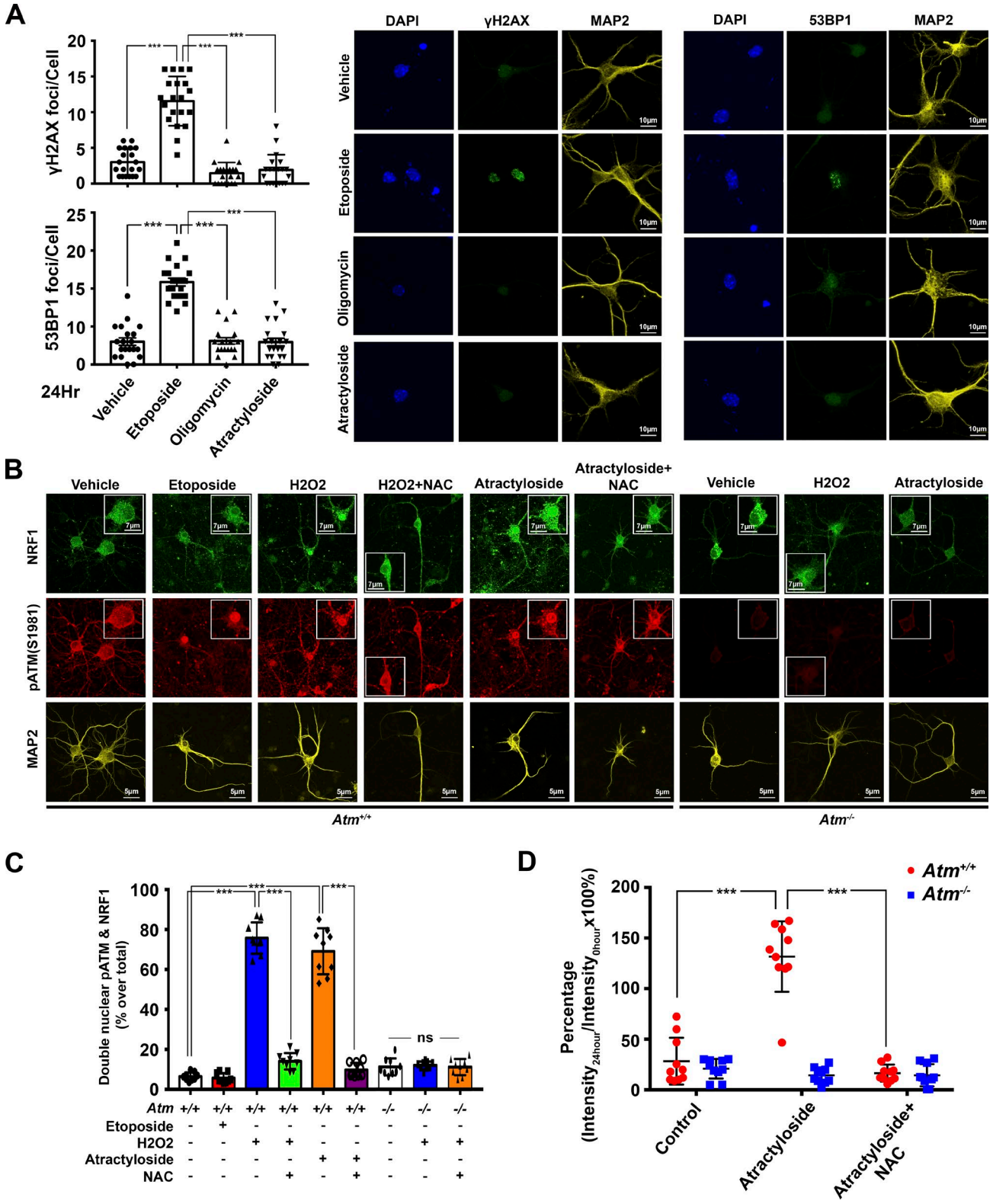

Figure 7. **ATP depletion activates ATM with downstream effects on NRF1. (A)** DIV 14 Primary cortical neurons isolated from WT mice were treated with vehicle, 1 µM etoposide, 0.5 µM oligomycin, or 1 µM atractyloside for 24 h. The number of γH2AX and 53BP1 foci in MAP2$^+$ neurons were then quantified (n = 20; ***, P < 0.001; one-way ANOVA). **(B)** Immunocytochemistry for activated ATM (pATM[S1981]), NRF1, and MAP2 (as indicated) in WT (*Atm*$^{+/+}$; left) and *Atm*$^{-/-}$ (right) DIV 14 primary cortical neurons treated with either vehicle, 1 µM etoposide, 10 nM H_2O_2, or 1 µM atractyloside in the presence or absence of 5 mM NAC for 24 h. **(C)** Quantification of the results in B (n = 9; ***, P < 0.001; ns, nonsignificant; one-way ANOVA). **(D)** NRF1-mediated transcription activities were measured using the NRF1mitoGFP reporter in WT DIV 14 primary cortical neurons, treated with either vehicle or 1 µM atractyloside in the presence or absence of 5 mM NAC. Intracellular GFP signals resulting from NRF1 transcription activity were monitored for 24 h after initiation of drug treatments. The ratios of cellular GFP intensities at 24- over 0-h time points are shown. Representative images of the reporter signals at 0- and 24-h time points can be found in Fig. S4 D.

point mutant clones at each of these sites confirmed the T259 residue as the relevant target of the ATM kinase (Fig. S5 A).

We further explored the nature of NRF1 dimerization in silico. While the structural features of the entire NRF1 protein have not yet been identified, we used ICM-Pro Browser to superimpose the Phyre[2]-predicted structure of the NRF1 dimerization domain (DIM) onto the bromodomain-containing protein-2/4 (BRD2/4; Garcia-Gutierrez et al., 2012). The fit suggested that the DIM domain of NRF1 closely resembles a bromodomain (Fig. 8, H and I). In silico phosphorylation of T259 followed by ZDOCK docking and contact area analyses with ICM-Pro Browser suggested a more favorable interaction between monomers phosphorylated at T259 than between nonphosphorylated monomers (Fig. 8 J and Table S1, M and N), consistent with the idea that T259 phosphorylation is a post-translational modification that triggers homodimerization (Fig. 8 K and Fig. S5 B). We separately verified the impact of NRF1 phosphorylation on nuclear-cytoplasmic shuttling (Fig. 8, L and M). Expression of a phosphomimetic mutant of NRF1 (T259E) promoted its nuclear localization, while expression of nonphosphorylatable NRF1 (T259A) led to a more prominent cytoplasmic localization in primary neurons. As expected, nuclear localization of WT NRF1 was lost if cells were pretreated with ATM inhibitor (Fig. 8, L and M). We also validated the importance of ATM activity (Fig. S5, C and D), specifically the activity induced by oxidative stress (Fig. S5 E), as mediating the phosphorylation, dimerization, and nuclear localization of NRF1.

Ectopic expression of T259E NRF1 rescues bioenergetic defects in *Atm*$^{-/-}$ neurons

To confirm that NRF1 is the downstream effector of ATM in sustaining mitochondrial bioenergetics and that the NRF1 T259 phosphorylation site plays an indispensable role in mediating mitochondrial dysfunction and ATP insufficiency in A-T, we ectopically expressed either the phosphomimetic T259E or nonphosphorylatable T259A mutants of NRF1 in neurons for 96 h before an array of mitochondrial analyses. Real-time PCR revealed that NRF1-T259E, but not T259A, rescued the reduced mRNA expression of most nuclear-encoded mitochondrial respiratory genes in *Atm*$^{-/-}$ cells (Fig. 9 A). This rescue effect was subsequently reflected in multiple mitochondrial functions, including static (Fig. 9, B and C) and dynamic (Fig. 9, D and E) mitochondrial potential; reserved respiration capacity (Fig. 9 F); static levels of ATP (Fig. 9 G); and dynamic ATP recovery rate (Fig. 9, H–J). None of the restorative effects of the NRF1-T259E mutant were seen with the nonphosphorylatable NRF1-T259A mutant (Fig. 9 K). Conversely, using *Atm*$^{+/+}$ neurons, we confirmed that NRF1 nuclear activities depend on ATM activity (Fig. 9, L and M), mediated by specific phosphorylation of the T259 residue, even in the presence of functional ATM, presumably due to a dominant-negative activity from overexpression of nonphosphorylatable T259A (Fig. 9 N).

Discussion

Our data present an expanded relationship between the ATM kinase and mitochondrial function and offer a new perspective on the reasons for symptoms in persons with A-T. We have found that, separate from the DNA damage response, ATM also functions as a sensor and regulator of a broad cellular response that integrates energy demand and mitochondrial biosynthesis. This newly identified ATM function is particularly important in large, energy-intensive cells such as Purkinje cells. The key to the new pathway is the ATM-mediated phosphorylation of NRF1. A linkage between ATM and mitochondria was first proposed by the Kastan laboratory (Valentin-Vega et al., 2012), who reported that ATM-deficient fibroblasts had defective mitophagy. Fang et al. (2016), extended this line of investigation, showing that impaired mitophagy resulted from ATM deficiency is contributed by the PARP1–NAD$^+$–SIRT1 pathway. Other researchers have also reported on the importance of ATM in the regulation of mitochondrial function (Zakikhani et al., 2012; Morita et al., 2014; Aird et al., 2015; Fang et al., 2016). None of these earlier studies, however, focused on the more fundamental linkage between ATM and cellular energy levels.

Our results indicate that a key linkage between ATM and mitochondrial function is through ATP itself, specifically the oxidative stress generated during ATP insufficiency. If this situation persists, a cell responds by increasing its mitochondrial content. This requires enhanced transcription from dozens of nuclear-encoded genes whose protein products take part in mitochondrial biogenesis. This response is critical to cell viability and thus is regulated by several intersecting pathways which appear to share ROS as an activating trigger. For example, chronic ATP insufficiency also results in intracellular calcium increase (Le Masson et al., 2014), which activates multiple extramitochondrial ROS-generating enzymes (Yan et al., 2006). In a similar vein, cytosolic glutathione, a cellular ROS scavenger (Hargreaves et al., 2005), is synthesized de novo by two sequential enzymatic ATP-dependent reactions (Chen et al., 2005). In this and possibly other cases, reduced ATP levels lead to increased ROS. Here, we revealed that ATM is activated by the increased ROS levels caused by the insufficiency of cellular ATP. Activated in this way, ATM phosphorylates and activates NRF1, the master regulator of nuclear encoded mitochondrial genes, at the T259 residue. This newly recognized ATM response system is only revealed when the cell is under conditions of stress. It is only when the $\Delta\psi m$ is completely depolarized with FCCP or when the cells are challenged with a massive energy demand, such as that following a prolonged depolarization, that the homeostatic failure of *Atm*$^{-/-}$ cells with regard to their ATP levels becomes apparent.

This scenario of sustained ATP deficiency causing ATM-dependent activation of NRF1-related gene transcription offers fresh insight into why cerebellar ataxia manifests as the most prominent neurological phenotype of human A-T. Here the explanation seems to lie in both the physiology of the Purkinje cell and the expression pattern of NRF1. Purkinje cells, with their large cellular size and vast number of synaptic inputs (Sugimori and Llinás, 1990; Welsh et al., 2002; Carter and Bean, 2009), are the only efferent neurons of the cerebellar cortex. Computational modeling predicts that each Purkinje cell consumes 62 times more energy than each cerebellar granule cell and 3.9 times more than a cortical pyramidal neuron (Fig. 8 N and Table S1 O). Most of this energy is used to run the Na^+/K^+ pumps that restore the neuronal membrane potential after an action potential (Fig. 8 N and Table

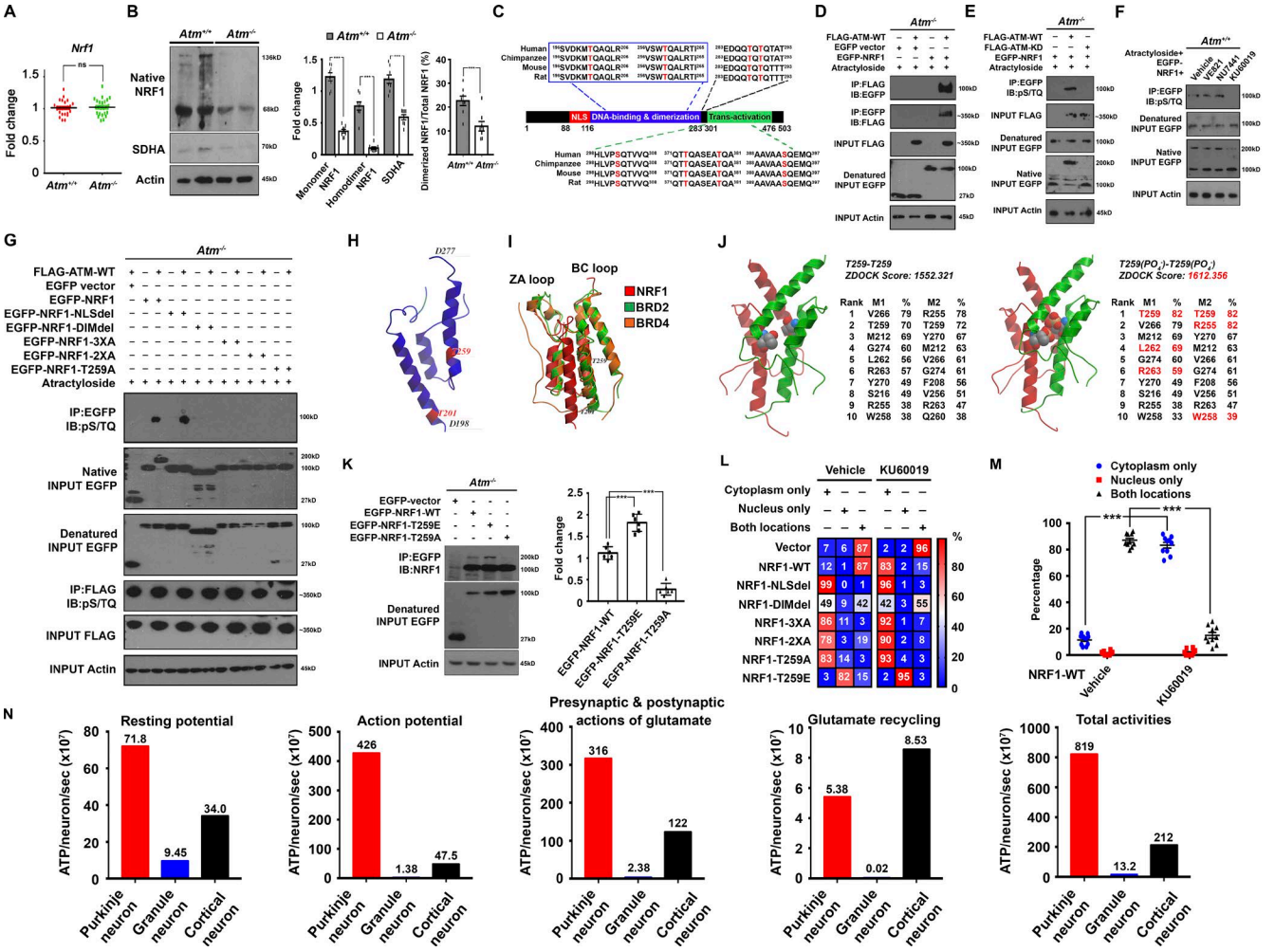

Figure 8. **ATM-mediated phosphorylation of the NRF1 T259 residue facilitates homodimerization and nuclear localization. (A)** *NRF1* gene expression in mouse cerebellum (n = 28–30; ns, nonsignificant; unpaired t test). **(B)** Representative Western blot and quantification in mouse cerebellum (n = 4; ***, P < 0.001; unpaired t test). **(C)** NRF1 protein sequence alignment, performed on the Clustal Omega platform. **(D–F)** Representative Western blots of immunoprecipitates showing interactions between NRF1 and ATM. Reciprocal immunoprecipitates of EGFP-NRF1 and FLAG-ATM-WT (D); (S/T)Q phosphorylation (top) and dimerization of EGFP-NRF1 mediated by WT, but not KD ATM (E); inhibition of ATM (with KU60019), but not ATR (with VE821) or DNA-PKcs (with NU7441), blocks (S/T)Q phosphorylation of EGFP-NRF1 in MEFs (F). **(G)** Western blot images showing that both T259 phosphorylation and nuclear localization are required for NRF1 homodimerization (n = 4). **(H)** NRF1 (aa 198–271) structure is predicted to adopt a bromodomain configuration in the region of its DNA-binding and dimerization domain. **(I)** This region of NRF1 (red) superimposes well with BRD2 (green) and BRD4 (orange) bromodomains. **(J)** In silico site-directed mutagenesis was performed to obtain the T259($PO4^-$) structure, followed by homodimer docking analyses using the ZDOCK platform. Predicted homodimerized best-ranking NRF1 bromodomain structures are shown in the table. Contact area analysis was performed; amino acid residues that showed significant interactions between the monomers were ranked. **(K)** Western blots of GFP-tagged NRF1 coimmunoprecipitations. Quantification of the percentage of dimerized NRF1 is shown (n = 6; ***, P < 0.001; one-way ANOVA). **(L)** Nuclear versus cytoplasmic localization of NRF1 mutants expressed in DIV 12 primary cortical neurons as shown in a heat map. **(M)** Distribution of EGFP-NRF1-WT proteins in neurons treated with 1 µM KU60019 for 96 h (n = 10; ***, P < 0.001; one-way ANOVA). **(N)** Histograms showing ATM requirements of individual Purkinje (red), cerebellar granule (blue), or cortical pyramidal (black) neurons. Individual panels show energy consumption by specific subcellular processes as marked. Parameters and calculations as per Howarth et al. (2012), details can be found in Table S1 O. IB, immunoblot; IP, immunoprecipitate.

S1 O; Howarth et al., 2010, 2012). Purkinje cells spike at high frequency, resulting in almost twice the amount of sodium entering during each spike, as compared to the theoretical amount predicted based on the kinetics of a single action potential. However, only 25% extra sodium influx was found in the case of slow-spiking pyramidal neurons (Carter and Bean, 2009). This implies that more energy needs to be consumed by the Na^+/K^+ pumps to restore ion gradients in Purkinje cells. With their extraordinarily high metabolic and ATP demands, it follows that Purkinje cells are exquisitely vulnerable to oxidative stress and metabolic insufficiency (Sugimori and Llinás, 1990). Indeed, explanation for the unique impact of ATM deficiency on the Purkinje cell is further supported by regional variations in the NRF1 protein itself. Our data showed that NRF1 is enriched in Purkinje cells; as others also revealed that a CNS-targeted NRF1 knockout results in selective Purkinje cell loss and motor ataxia (Kobayashi et al., 2011).

Our findings regarding the cellular ATP dynamics can also be seen in the context of immediate ATP level regulations by the AMP-activated protein kinase. Comparing the AMP-activated protein kinase response to that of ATM suggests the latter, with

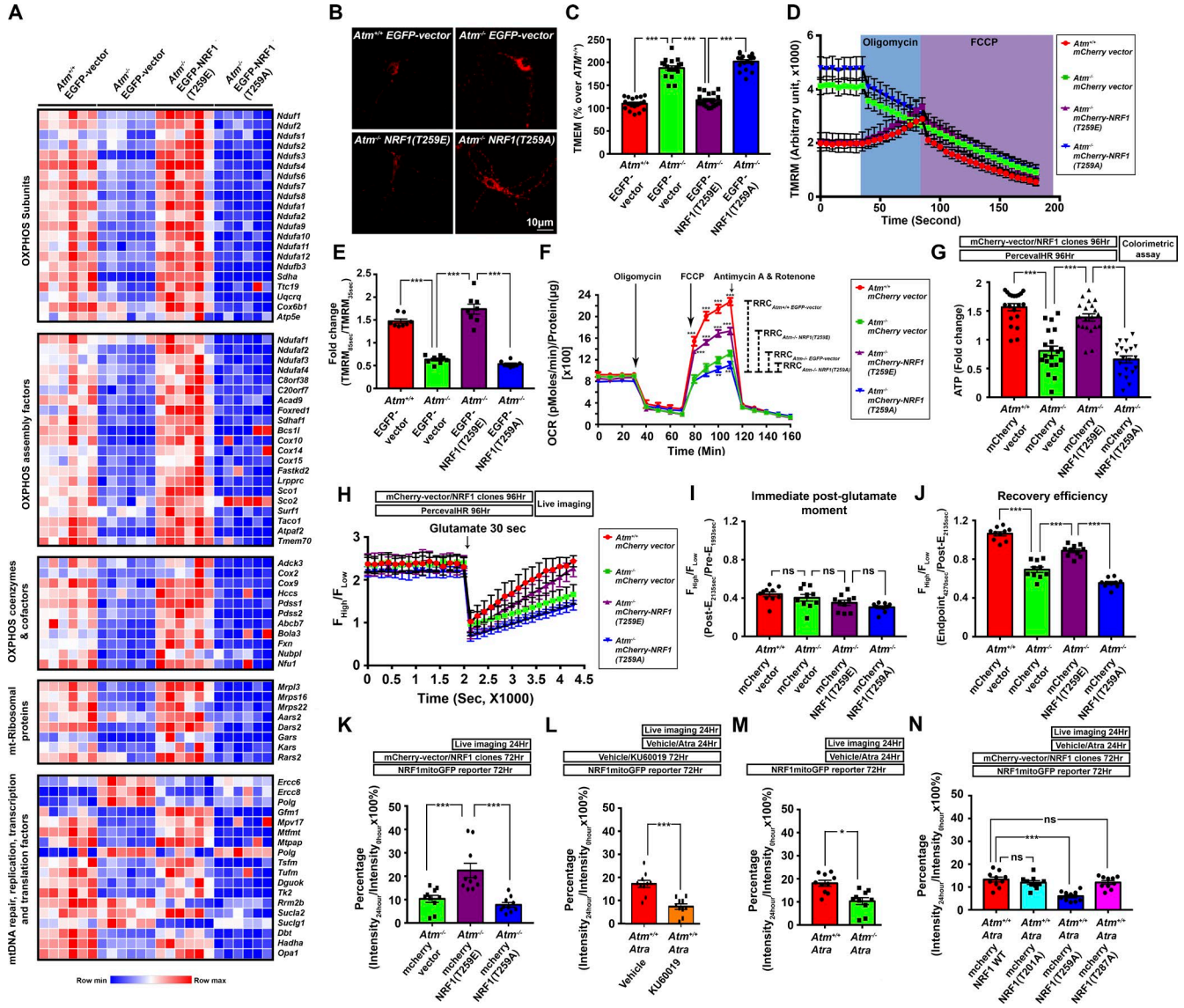

Figure 9. **Ectopic expression of T259E NRF1 rescues bioenergetic defects in *Atm*$^{-/-}$ neurons. (A)** Heat maps indicating mRNA expression of 79 nuclear-encoded genes whose loss of function is associated with neurodegeneration (n = 6 biological samples; n = 3 technical replicates). **(B–D)** Static (n = 18; ***, P < 0.001; one-way ANOVA; B and C) and dynamic changes (D) in mitochondrial membrane potential in primary cortical neurons were evaluated with TMRM (n = 8). **(E)** The relative changes in TMRM signals in cells expressing the indicated constructs in the genotypes as shown. TMRM signal was expressed as the ratio of postoligomycin (85 s) to preoligomycin (35 s) OCR values (n = 8; ***, P < 0.001; one-way ANOVA). **(F)** Seahorse Mito Stress assay in neurons preexpressing the indicated NRF1 constructs for 96 h (n = 10; ***, P < 0.001; **, P < 0.01 two-way ANOVA). **(G and H)** Static and dynamic changes in ATP levels in primary cortical neurons were measured by the Perceval HR reporter. **(G)** Equilibrium ATP levels at the instant prior the dynamic experiment was measured by colorimetric assay (n = 20; ***, P < 0.001; unpaired t test). **(H)** Live imaging of cultured neuron responses to 50 µM glutamate effects on energy consumption. After establishing a steady baseline, glutamate was added for 30 s and then washed away, and intracellular ATP levels allowed to recover (n = 10; ***, P < 0.001; two-way ANOVA). **(I and J)** The relative abundance of ATP/ADP immediately following the removal of glutamate (Signal ratio: Post-$E_{2135sec}$/Pre-$E_{1993sec}$; I) and after recovery (Signal ratio: Endpoint$_{4,270sec}$/Post-$E_{2,135sec}$; J; n = 10; ***, P < 0.05; ns, nonsignificant; unpaired t test). **(K–N)** NRF1-mediated transcription activities were monitored by the NRF1mitoGFP reporter. *Atm*$^{-/-}$ neurons preexpressed the indicated forms of NRF1 for 72 h (n = 10; ***, P < 0.001; one-way ANOVA; K). Loss of neuronal ATM activity by either treatment of WT cells with 1 µM KU60019 for 96 h (n = 10; ***, P < 0.001; unpaired t test; L) or treatment of genetically *Atm*$^{-/-}$ cells (n = 10; *, P < 0.05; unpaired t test; M) reduced NRF1-reporter activities. **(N)** Loss of ATM-induced NRF1 reporter activities by 1 µM atractyloside treatment (24 h) is specific to the NRF1-T259A mutant, but not point mutants at T201 or T287 (n = 10; ns, nonsignificant; ***, P < 0.001; one-way ANOVA). For assays in K–M, intracellular GFP signals resulting from NRF1 transcription activity were monitored for 24 h after the initiation of atractyloside treatments. For K–M, ratios of cellular GFP intensities are shown at 24 h over 0 h time points.

its requirement for significant ROS signaling, ensures a structural and more sustained response to large, chronic changes in ATP. Although it has been suggested that the neurodegenerative phenotype of A-T is mainly attributable to inefficient DNA repair, some studies reveal that A-T cells exhibit normal levels of DNA repair (Kastan and Lim, 2000), despite being slower. Further, DNA damage is mostly a stochastic event that occurs throughout the genome of all cells; it is difficult to explain how such randomness confers to the selective loss of Purkinje cells in all A-T patients. Combining the predicted energy demands unique to

Purkinje cells, with a defective capacity to respond to the drop in ATP levels brought on by high levels of neuronal activity, makes the neurological symptoms of A-T seem much less puzzling.

Materials and methods

Reagents, primers, and algorithms

Details of antibodies, chemicals and assay kits are listed in Table S2 A. Sequence-based reagents, including primers for real-time PCR and site-directed mutagenesis are listed in Table S2 B. For details regarding software and algorithms used in this study, please refer to Table S2 C.

Mitochondrial database

Associations between various symptoms of A-T were generated using the online database MitoDB (Scheibye-Knudsen et al., 2013). On the home page of the database, A-T was chosen as the disease to be tested. Once test results were generated, the number of mitochondrial versus nonmitochondrial diseases (including those in the "Unknown" category) associated with different symptoms of A-T were tabulated on the subpage named "Barcode." Details of the data can be found in Table S1 A.

Multiple protein sequence alignment

Protein sequences of NRF1 in *Homo sapiens* (human; NP_001035199.1), *Pan troglodytes* (chimpanzee; XP_001155812), *Mus musculus* (mouse; NP_035068.3), and *Rattus norvegicus* (rat; NP_001094178.1) were obtained from the NCBI Gene database. Multiple protein sequence alignment was performed on the Clustal Omega platform. Conserved (S/T)Q sites among all the species analyzed were manually identified for subsequent analysis.

Human microarray data mining

A human expression array dataset (Gene Expression Omnibus accession no. GSE61019), comparing samples of A-T and control cerebella (Jiang et al., 2015), was analyzed with GEO2R. Raw data from each of the samples were extracted.

GO analysis

All transcripts that reflected significant changes (adjusted $P \leq 0.05$) by the GEO2R analyzer were extracted (Table S1 B, yellow highlights) and analyzed on the GATHER platform (Chang and Nevins, 2006). Among all 30 GO terms that reflected the greatest possible significance ($P < 0.0001$), we performed enrichment analysis (listed in descending order) based on the corresponding Bayes factors (BFs) and the number of genes indicated in each GO term.

GSEA

We performed a second analysis using GSEA with the KEGG pathway groupings of genes (Subramanian et al., 2005). The full list of phenotypes enriched in the normal can be found in Table S1 E. Pathways with normalized $P < 0.01$ are highlighted in yellow.

Human MitoCarta2.0 analysis

We performed a third analysis using MitoCarta2.0, a collection of 1,158 nuclear and mitochondrial genes encoding proteins with strong evidence for mitochondrial localization (Calvo et al., 2016). The matching genes were extracted from the raw dataset of this human array for expression analysis. The full list of extracted data from each individual sample can be found in Table S1 F. Table S1 G contains the comparison data between the control versus A-T groups. Specific genome localization of each gene was also determined. Note that a list of 42 genes from the MitoCarta2.0 list failed to match probes on the human expression array.

PSCAN gene promoter analysis

To identify potential transcription factors that result in global changes of gene expression, we used the PSCAN platform (Zambelli et al., 2009) to analyze the genes identified in the human expression array data that showed significant differences of expression between A-T and control cells. The list of gene IDs was first converted to the corresponding RefSeq mRNA IDs using the DAVID platform (Huang da et al., 2009) and subsequently input into PSCAN, using the "human and mouse" species option; a default promoter setting of "−450 to +50" was used to cover the regions located immediately adjacent to the transcription start site. The JASPAR 2014 matrices were also selected for analysis. The results are compiled in Table S1 J. Detailed matrix information, sample mean score, and statistics are listed for each site of interest. *NRF1* was the gene that ranked highest in this analysis and was thus subjected to further scrutiny. The list of NRF1-binding sites in each input promoter, with corresponding gene name, oligo score, and position with respect to transcription start site of the gene, oligo sequence, and strand were extracted for further analysis.

In silico protein structure modeling, docking, and contact area analysis

With the protein sequence of the human NRF1 protein (NP_001035199.1) obtained from the NCBI-Gene database, the DNA binding and dimerization domain (aa 116–283) was used to predict the corresponding 3D protein structure on the Phyre^2 engine, using the intensive modeling mode (Kelley et al., 2015). The highest-ranking model (with score >85), was used to overlap the excised bromodomain structures of BRD2 (Protein Data Bank: 5UEW) and BRD4 (Protein Data Bank: 4O76) on Molsoft ICM-Pro Browser, or directly adopted for subsequent in silico docking analysis for the homodimerized NRF1 structure on the ZDOCK server (Pierce et al., 2014). The best-ranked model (with the highest ZDOCK score) from each analysis was then subjected to contact area analysis for visualizing interacting amino acid residues with the Molsoft ICM-Pro Browser. To evaluate the monomer structures, T259 was mutated to T259(PO_4^-) using Pymol mutagenesis tool before the same docking procedures and contact area analysis.

Animal maintenance, brain tissue isolation, and primary neuronal and MEF culture

C57BL/6J and 129S6/SvEvTac-Atmtm1bal/J (heterozygous for an engineered ATM kinase domain mutation; Xu et al., 1996) were obtained from The Jackson Laboratory. Colonies were maintained in the Animal and Plant Care Facility of the Hong Kong University of Science and Technology (HKUST). Homozygous mutants ($Atm^{-/-}$) were generated by mating heterozygous

carriers ($Atm^{+/-}$), as per The Jackson Laboratory protocol. All animal experimental protocols were approved by the Animal Ethics Committee at HKUST, and their care was in accord with the institutional and Hong Kong guidelines.

Brain tissue was isolated by anesthetizing adult mice with intraperitoneal administration of 1.25% (vol/vol) Avertin at a dosage of 30 ml/kg body weight. The heart of each mouse was then surgically exposed, the left chamber was catheterized, and the right atrium was opened. Chilled physiological saline was perfused transcardially for 3 min to remove blood from the body. After perfusion, the cranial bones were opened; cortex and cerebellum were harvested, snap-frozen in liquid nitrogen, and stored at −80°C until use.

Embryonic cortical neurons were isolated by standard procedures (Chow et al., 2014). Gravid females were killed on the 16th day of gestation and the embryonic day 16.5 (E16.5) embryos collected in ice-cold PBS-glucose. The cortical lobes were removed, following which the meninges were removed, and the cortices were placed in 1× trypsin solution for 10 min, with manual shaking at 5 min. After digestion, an equal volume of DMEM with 10% (vol/vol) FBS was added to inactivate the trypsin. Samples were then centrifuged at 2,500 rpm for 5 min. Supernatant was removed, followed by transferring the pellet to fresh Neurobasal medium supplemented with B-27, penicillin/streptomycin (1×), and L-glutamine (2 mM; GlutaMAX; Invitrogen) before gentle resuspension. Tissue was triturated 10 times through a 5-ml pipette and allowed to settle to the bottom of a 15-ml conical tube. Cells in solution above the pellet were removed. Surviving cells were identified by trypan blue exclusion and counted before plating on poly-L-lysine–coated (0.05 mg/ml) glass coverslips. Unless otherwise specified, cells were plated in 24-well plates at 50,000 cells per well and allowed to mature for over 7–10 d in vitro (DIV) before transfection or lentiviral transduction. For other experiments, cells were grown for a minimum of DIV 14 before drug treatment experiments. Every 3 d half of the culture medium was replaced with an equal volume of fresh medium to sustain the culture.

MEF cell cultures were established from the same E16 embryos used for isolation and culture of primary cortical neurons. After the heads (for primary neuronal culture), tails, limbs, and internal organs were removed, the remaining tissue was minced and trypsinized for 20 min, then seeded into P100 culture dishes in 12 ml of the complete MEF medium (Iscove's modified Dulbecco medium containing 10% iron-supplied calf serum [Hyclone], with additional nonessential amino acids, 2 mM GlutaMAX, and 1% Penicillin-Streptomycin). When cultures became confluent, the cells were split 1:2 or 1:3, then passaged two or three times to obtain a morphologically homogenous culture. At this point cells were harvested and separated into aliquots that were either frozen or expanded for further studies.

Postmortem human brain samples

Frozen postmortem brain samples of diseased A-T patients and age-matched controls were requested from the NeuroBioBank, National Institutes of Health (NIH). All samples were thoroughly anonymized prior distribution. The US Human Studies Board characterizes these tissues as exempt. All studies conducted using human tissue strictly complied with the ethical standard of NIH and the Ethics Committee on Research Practices of the HKUST. Frozen sections were prepared from brain blocks and were used for immunohistochemistry purposes. All tissue sections were examined and imaged on a fluorescent microscope (Olympus BX53 with DP80 camera) equipped with 20× (UPlanSApo; 0.75 NA) objective, using an X-Cite 120Q light source (Excelitas Technologies Corp.).

Cell culture and transfection

Lines of primary human skin fibroblasts from A-T patients and their respective controls were obtained from the NIA Aging Cell Repository of the Coriell Institute for Medical Research and maintained in DMEM/10% FBS. Primary neurons were isolated from E16 embryos of C57BL/6J or $Atm^{+/-}$ pregnant mice and cultured as described above. DNA constructs were transfected with Lipofectamine LTX in the presence of Plus Reagent into both types of primary culture following the manufacturer's protocol. At 5 h after transfection, cells were refreshed with new culture medium (or conditioned medium for primary neurons) and further incubated for 48–72 h to allow recovery and ectopic expression of transfected constructs.

Lentivirus production and transduction

Lentivirus stocks were produced as previously described with slight modifications (Cribbs et al., 2013). Human embryonic kidney 293FT cells (Invitrogen) were transfected using Lipofectamine 2000 (Invitrogen) with the expression of two helper plasmids: psPAX2 and pMD2.G. 10 µg transfer vector, 5 µg pMD2.G, and 5 µg psPAX2 of DNA were used per 10-cm plate. 48 h after transfection, the supernatants of four plates were pooled, centrifuged at 780 *g* for 5 min, filtered through a 0.45-µm pore size filter, and further centrifuged at 24,000 rpm for 2 h. The resulting pellet was resuspended in 100 µl of PBS. Lentivirus titration was performed with a p24 ELISA (Clontech).

Coimmunoprecipitation, SDS-PAGE-Western Blotting, and native PAGE-Western blotting

Isolated brain tissues or cell pellets were homogenized in radioimmunoprecipitation assay buffer (Millipore) with 1× complete protease inhibitor mixture (Roche) and 1× PhosSTOP phosphatase inhibitor mixture (Roche) on ice, then centrifuged for 10 min at 18,400 *g* to remove large debris. The protein concentration of the supernatant was determined by Bradford Assay (Bio-Rad). For coimmunoprecipitation, 1 mg of the total cell lysates was first incubated with control IgG (Santa Cruz Biotechnology) for 30 min, precleared with 50 µl Dynabeads Protein G (Invitrogen), and then incubated with various antibodies overnight at 4°C, using the suggested dilutions from the product datasheets. Beads bound with immune complexes were collected by DynaMag-2 (Life Technologies) and washed three times before elution in 90 µl of buffer containing 0.2 M Glycine-HCl, pH 2.5, which was neutralized with 10 µl of neutralization buffer (1 M Tris-HCl, pH 9.0). The eluates were subjected to 9–15% SDS-PAGE and Western blot analysis.

For SDS-PAGE, 100 µg of proteins derived from cell or tissue lysates was prepared in 5× sample buffer (10% wt/vol SDS, 10 mM β-mercaptoethanol, 20% vol/vol glycerol, 0.2 M Tris-HCl, pH6.8, and 0.05% Bromophenol blue). With a Bio-Rad system, separating gels of different acrylamide percentages (6–15%) were prepared

with the following components in double distilled water: acrylamide/bis-acrylamide (30%/0.8% [wt/vol] 1.5 M Tris, pH 8.8, 10% [wt/vol] SDS, 10% [wt/vol] ammonium persulfate, and tetramethylethylenediamine; TEMED) and a 5% stacking gel (5 ml prep: 2.975 ml water, 1.25 ml 0.5 M Tris-HCl, pH 6.8, 0.05 ml 10% [wt/vol] SDS, 0.67 ml acrylamide/bis-acrylamide [30%/0.8%; wt/vol], 0.05 ml 10% [wt/vol] ammonium persulfate, and 0.005 ml TEMED) were prepared. Samples were run in SDS-containing running buffer (25 mM Tris-HCl, 200 mM Glycine, and 0.1% [wt/vol] SDS) until the dye front and the protein marker reached the foot of the glass plate. Standard immune-blotting procedures were used, which include protein transfer to polyvinylidene difluoride membranes, blocking with nonfat milk, and incubation with primary and secondary antibody, followed by visualization with the SuperSignal West Dura/Femto Chemiluminescent Substrate (Thermo Fisher).

For native-PAGE, the same discontinuous chloride and glycine ion fronts as SDS-PAGE were used to form moving boundaries that stack and then separate polypeptides by their charge to mass ratio. Proteins (100 µg) were prepared in a nonreducing, nondenaturing sample buffer (2×: 62.5 mM Tris-HCl, pH 6.8, 25% glycerol, and 1% Bromophenol blue) without heating to maintain secondary structure and native charge density. With a Bio-Rad system, 10 ml/gel 8% native PAGE separating gel (2.6 ml acrylamide/bis-acrylamide [30%/0.8%; wt/vol], 7.29 ml 1.5 M Tris-HCl, pH 8.8, 100 µl 10% [wt/vol] ammonium persulfate, and 10 µl TEMED) and 5 ml/gel native PAGE stacking gel (4.275 ml 0.5 M Tris-HCl, pH 6.8, 0.67 ml acrylamide/bis-acrylamide [30%/0.8%; wt/vol], 0.05 ml 10% [wt/vol] ammonium persulfate, and 5 µl TEMED) were prepared. Samples were run in a nondenaturing running buffer (25 mM Tris and 192 mM glycine, pH 8.3) with the entire system cooled with ice. After electrophoresis, standard immune-blotting procedures were followed as above.

Quantitative real-time PCR (qPCR) analysis

Total cellular RNA was purified from brain cortex tissues or cultured cells using the RNeasy mini kit (Qiagen) following the manufacturer's protocol. For qPCR, RNA was reverse-transcribed using the High-Capacity cDNA Reverse Transcription kit (Applied Biosystems) according to the manufacturer's instructions. The resulting cDNA was analyzed by qPCR using SYBR green PCR Master Mix (Applied Biosystems). All reactions were performed in a Roche LightCycler 480 instrument using the following protocol: preincubation at 95°C for 15 min (1 cycle). denaturation at 94°C for 15 s, annealing and extension at 55°C for 30 s (40 cycles), melting at 95°C for 5 s, 65°C for 60 s, and 95°C continues (1 cycle), followed by cooling at 40°C for 30 s. The specificity of the primers was confirmed by observing a single melting point peak. qPCR efficiency was calculated from the slope was between 95 and 105% with coefficiency of reaction R^2 = 0.98–0.99. A total of seven to nine biological replicates by four technical replicates were performed for each treatment group. Data were analyzed using the comparative Ct method (ΔΔCt method).

Mitochondrial complex activity assays

Activities of Complexes I–IV were measured using kits purchased from BioVision (K968-100, K660-100, K520-100, and K287-100) and that of Complex V was measured using a kit from Invitrogen (KHM2051). Measurements were conducted by strictly adhering to the manufacturers' instructions.

Imaging intracellular pyruvate level in single cells with the FRET sensors, Pyronic and Laconic

Pyruvate sensor, Pyronic (Pyruvate Optical Nano-Indicator from Centro de Estudios Cientificos), was obtained from Addgene (plasmid no. 51308) as was the lactate sensor, Laconic (LACtate Optical Nano Indicator from CECs; Addgene; plasmid no. 44238). For both sensors, the exposure of the sensor to its ligand (pyruvate or lactate) causes an increase in monomeric TFP (mTFP; donor) fluorescence intensity and a decrease in Venus (mCFP, receiver) fluorescence intensity, thus resulting in a decrease in FRET efficiency. As reported previously (San Martín et al., 2014), the biosensors were transfected into cortical neurons on DIV 9. 24 h after transfection, cells were exposed to one of the following drug conditions.

For Pyronic: (1) vehicle (saline); (2) 30 mM 2-DG (Saraiva et al., 2010); (3) 1 µM UK5099 (Jourdain et al., 2016); or (4) 2.5 mM oxamate (Choi et al., 2012) in KRH-bicarbonate buffer (112 mM NaCl, 1.25 mM $CaCl_2$, 1.25 mM $MgSO_4$, 1–2 mM glucose, 10 mM Hepes, 24 mM $NaHCO_3$, pH 7.4, and 3 mM KCl).

For Laconic: (1) vehicle (saline); (2) 500 µM pCMBS (San Martín et al., 2014); or (2) 2.5 mM Oxamate (Choi et al., 2012) in imaging buffer (112 mM NaCl, 1.25 mM CaCl2, 1.25 mM MgSO4, 1–2 mM glucose, 10 mM Hepes, and 24 mM NaHCO3, pH 7.4, with 3 mM KCl).

Cultures were then live imaged for another 24 h with imaging at 6 h intervals in a 95% air/5% CO_2-gassed incubator using a Leica TCS SP8 confocal laser scanning platform equipped with Leica HyD hybrid detector and visualized through a HC PL APO CS2 63× (1.40 NA) oil-immersion objective. Image acquisition was controlled by the Leica Application Suite X Microscope Software (LAS X). To perform nanosensor ratio measurements, cells were excited at 430 nm for 0.2–0.8 s. Emission was divided with an Acousto-Optical Beam Splitter (Leica) on the same set up as mentioned above and recorded at 480 ± 20 (mTFP) and 535 ± 15 nm (Venus). The ratio between mTFP and Venus along time was used to estimate pyruvate concentrations inside the cell. The maximum z projection of the optical stacks is presented.

Colorimetric assay

Cellular contents of pyruvate were measured using kits purchased from BioVision (K609-100) following the manufacturers' instructions. Cellular contents of lactate were measured using specific kits purchased from BioVision (K607-100), following the manufacturer's instructions.

Cytosol and mitochondria separation followed by isocitrate and succinate colorimetric assays

pMX-3×FLAG-EGFP-OMP25 plasmid was obtained from Addgene (plasmid no. 83354). Human primary fibroblasts were first transfected with the plasmid as described above. In cases where the transfection efficiencies were ≥80%, after 72 h mitochondria were harvested by immunopurification (Chen et al., 2016b). 3×FLAG-EGFP-OMP25–expressing cells were gently scraped into

1 ml potassium-containing PBS (136 mM KCl and 10 mM KH_2PO_4, pH 7.25). The cell suspension was centrifuged at 1000 *g* for 2 min, supernatant was discarded, and the cell pellet gently resuspended in 1 ml of the kit-supplied assay buffer. Cells were homogenized with 25 strokes in a 2-ml Dounce homogenizer, taking care not to introduce air bubbles into the solution. The homogenate was then centrifuged and the mitochondria isolated by anti-FLAG immunoprecipitation (the entire procedure was performed on ice in a 4°C cold room with prechilled buffers and equipment). To increase the speed of isolation, only one sample for one metabolite analysis was processed at a time. Anti-FLAG magnetic beads (200 µl) were prewashed three times with KPBS by gentle pipetting using a wide-bore pipette tip. Beads were collected using a DynaMag (Thermo Fisher). Sample was then added to the beads and the mixture incubated overnight. The following day, antibody-bound mitochondria were separated from the cytosol using the DynaMag; the cytosol fraction was saved for metabolite analysis. The isolated beads were quickly washed twice with 1 ml KPBS, resuspended in 1 ml assay buffer, and transferred to a new tube. An aliquot of the mitochondrial suspension (250 µl) was taken for detergent lysis and protein quantification; the remainder was used for metabolite extraction analyses.

Cytosolic and mitochondrial contents of isocitrate and succinate were measured using kits purchased from BioVision (K656-100 and K649-100, respectively).

Live imaging of cytoplasmic redox status

Cyto-roGFP obtained from Addgene (plasmid no. 49435) senses redox changes in a cell (Waypa et al., 2010). The Cyto-roGFP biosensor was transfected into cortical neurons on DIV 9, and 24 h after transfection, neurons were exposed to one of the following conditions: (1) vehicle (saline); (2) 10 nM H_2O_2 (Wang et al., 2007); or (3) 1 µM atractyloside (Schütt et al., 2012) in Neurobasal culture medium. Cultures were then imaged for 24 h at hourly intervals in a 95% air/5% CO_2-gassed incubator using a Leica TCS SP8 confocal laser scanning platform, equipped with Leica HyD hybrid detector and visualized through a HC PL APO CS2 63× (1.40 NA) oil-immersion objective. Image acquisition was controlled by LAS X. The redox-sensitive protein reporter has excitation maximum at 400 ± 15 nm and 484 ± 15 nm and an emission maximum at 525 ± 15 nm. The relative amplitudes of these peaks depend on the state of oxidation. With increased oxidation the 400 ± 15-nm excitation peak increases, while the 484 ± 15-nm peak decreases (Hanson et al., 2004). Importantly, the ratiometric nature of the analysis renders the results independent of the expression levels of the plasmid in any one cell. Data were collected with the Leica Application Suite X Microscope Software. The fluorescence excitation ratios were obtained by dividing integrated intensities obtained from manually selected portions of the imaged regions of intact whole cells collected using 400 ± 15-nm and 480 ± 15-nm excitation filters after appropriate background correction. Background correction was performed by subtracting the intensity of a nearby cell-free region from the signal of the imaged cell.

Imaging intracellular ATP/ADP ratio

Perceval High Range (PercevalHR) obtained from Addgene (plasmid no. 49082) senses changes in the ATP/ADP ratios in mammalian cells (Tantama et al., 2013). We transfected PercevalHR into cortical neurons on DIV 9. 24 h after transfection, neurons were imaged on a Carl Zeiss AxioOberver Z1 Inverted Microscope with a piezo Z-stage glass slide insert. The sensor has two distinct peaks of excitation; ATP binding increases the fluorescence at 500 nm, while ADP increases fluorescence at 420 nm. PercevalHR was excited sequentially using 482 ± 15–nm and 445 ± 15–nm band pass filters; emission was measured with a 529 ± 15–nm band pass filter. The excitation and emission signals were optically separated with a 490-nm short pass dichroic mirror. Images were taken over a period of 72 min (capture time, 2 min). The ratio of the fluorescence signal at the two different excitation wavelengths (F_{high}/F_{low}) reports the ATP occupancy of the reporter and is independent of the amount of sensor protein in the cell.

During the imaging process, neurons were placed in a custom chamber which was continuously perfused with a bathing solution (2 ml/min; 32–34°C) containing 120 mM NaCl, 3 mM KCl, 2 mM $CaCl_2$, 1 mM $MgCl_2$, 3 mM $NaHCO_3$, 1.25 mM NaH_2PO_4, 15 mM Hepes, 5 mM glucose, 0.2 mM pyruvate, and 0.5 mM GlutaMax, adjusted to pH 7.4. We determined a baseline reporter signal by imaging a resting cell for at least 25 min. After ensuring a stable signal, 50 µM glutamate was applied for 30 s to strongly excite the neurons. Following the depolarization, the cell would need considerable amounts of ATP to drive the Na^+/K^+-ATPase (sodium pump) to be able to restore the resting ion gradients. We followed the drop in ATP and its subsequent restoration by the mitochondria for 30–45 min after the glutamate stimulus.

ATP colorimetric assay

The cellular contents of ATP were measured using kits purchased from BioVision (K354-100).

Determination of mitochondrial membrane potential

TMRM (Thermo Fisher) is a cell-permeant, cationic, red-orange fluorescent dye that is sensitive to the mitochondrial membrane potential; Mitotracker green (Thermo Fisher), a mitochondrial dye that is insensitive to $\Delta\psi m$, was used as a counterstain. Stock solutions of the dyes (10 mM) were prepared in anhydrous DMSO. Cultured cortical neurons or human fibroblasts were first washed thrice with Tyrode's buffer (145 mM NaCl, 5 mM KCl, 10 mM glucose, 1.5 mM $CaCl_2$, 1 mM $MgCl_2$, and 10 mM Hepes; adjusted to pH 7.4 with NaOH). Working concentrations (20 nM) of TMRM and Mitotracker green were prepared in Tyrode's buffer and applied to the cells. After incubation in dark at room temperature for 45 min, imaging was performed on Leica TCS SP8 confocal laser scanning platform equipped with Leica HyD hybrid detector and visualized through a HC PL APO CS2 63× (1.40) NA oil-immersion objective. Image acquisition was controlled by LAS X using the time-series and sequential scanning programs. TMRM was excited at 514 ± 15 nm and the emission at 570 ± 15 nm was measured. Mitotracker green was excited at 480 ± 15 nm and detected at 520 ± 15 nm. To test changes in mitochondrial membrane potential, 1 µM FCCP or 2 µg/ml of oligomycin, were applied, which depolarized or hyperpolarized the mitochondrial membrane potential, respectively (Joshi and Bakowska, 2011).

Assessment of mitochondrial function

The mitochondrial OCR in both primary neurons and human fibroblasts were assessed using a Seahorse Bioscience XF^{e}24 analyzer (Agilent) in combination with the Seahorse Bioscience XF Cell Mito Stress Test assay kit. In this assay, sequential additions of the ATP synthase inhibitor, oligomycin, the mitochondrial uncoupler, FCCP, and the complex I + II inhibitors rotenone + antimycin A provide insight into different aspects of mitochondrial function, as described in the text. Experiments were performed on intact adherent cells.

Coating and cell plating

The surface area of each well of the 24-well Seahorse XF24 microplate is identical to that of standard 96-well microplates (0.32 cm^2). Poly-L-lysine (0.1 mg/ml in sterile borate buffer, pH 8.4; 500 µl/well) was incubated overnight at 37°C, 5% CO_2, and 95% humidity. The substrate solution was then removed, and the microplates were dried without further rinsing under a sterile laminar flow hood. Dissociated primary cortical neurons were isolated as described above. 100,000 neurons/well or 80,000 primary fibroblasts/well were seeded in a volume of 150 µl. Immediately after seeding, plates were incubated for 1 h at 37°C prior to bringing the total volume of each well to 500 µl with corresponding culturing medium (Neurobasal medium for neurons; DMEM with 10% FBS for human fibroblast). Fibroblast cultures were maintained for 2 d before analysis. For neurons, after one night of settling, cultures were treated with 20 µM fluorodeoxyuridine in Neurobasal medium for 24 h with medium changed every other day; this method eliminates most of the nonneuronal cells. Neurons were maintained until DIV 7 before subsequent analysis.

Cell mito stress test assay

Growth medium was removed, leaving 50 µl in each well, after which cells were rinsed twice with 400 µl of prewarmed assay medium, consisting of XF base medium supplemented with 25 mM glucose, 2 mM glutamine, and 1 mM sodium pyruvate buffered to pH 7.4. Following the rinses, 475 µl assay medium and 50 µl conditioned medium (525 µl final) were added to each well. Cells were then incubated in a 37°C incubator without CO_2 for 1 h, after which prewarmed oligomycin, FCCP, rotenone, and antimycin A solution were loaded into injector ports A, B, and C of the sensor cartridge to achieve final concentrations of 0.5 µM for oligomycin, 1 µM for FCCP, and 1 µM for rotenone and antimycin A. The cartridge was calibrated with the XF24 analyzer, and the assay performed as described (Nicholls et al., 2010).

The OCR was measured and changes from baseline rates were tracked following the sequential addition of oligomycin, FCCP, and the rotenone + antimycin A mixture. This allowed for calculation of the basal respiration rate, proton leakage, maximal respiration, spare respiratory capacity, nonmitochondrial respiration, and ATP production (Nicholls et al., 2010) by Seahorse XF24 software version 1.8. At the end of each assay, cells were washed once with an excess of room temperature PBS, lysed with ice-cold radioimmunoprecipitation assay buffer (0.15 M NaCl, 1 mM EDTA, 1 mM EGTA, 0.5% sodium deoxycholate, 0.1% SDS, 1% Triton X-100, and 50 mM Tris-HCl, pH 8, with added protease and phosphatase inhibitor cocktails). Protein content was estimated by the Bio-Rad Dc protein assay (Bio-Rad), using a Molecular Devices Softmax M3 microplate reader (Sunnyvale). Data from each well were then normalized for total protein content. Normalized Seahorse XF^{e}24 measurements were used to calculate a mean (± SEM) for each density group and each plate using XF24 software version 1.8 (Seahorse Bioscience).

Table 1. **Metabolic tests and associated inhibitors**

Metabolite test	Treatment 1	Treatment 2
Glucose/Pyruvate dependence	UK5099	Etomoxir + BPTES
Glutamine dependence	BPTES	Etomoxir + UK5099
Fatty acid dependence	Etomoxir	BPTES + UK5099

Dependency (%) = ([Baseline OCR-Target inhibitor OCR]/[Baseline OCR-All inhibitors OCR]) × 100%.

Metabolic fuel flux assays

The Mito Fuel Flex Tests were performed on Seahorse XF^{e}24 Bio-analyzer (Agilent). All assays were performed following manufacturer's protocols. In brief, the test inhibits import of three major metabolic substrates (pyruvate, fatty acids, and/or glutamine) with mitochondrial pyruvate carrier inhibitor UK5099 (2 µM), carnitine palmitoyltransferase 1A inhibitor etomoxir (4 µM), or glutaminase inhibitor BPTES (3 µM). This test determines cellular dependence on each of the metabolites to fuel mitochondrial metabolism by inhibiting the individual substrate import. Baseline OCR was monitored for 18 min followed by sequential inhibitor injections (i.e., Treatment 1 or Treatment 2) with OCR reading for 1 h following each treatment. The inhibitor treatments and calculations are shown in Table 1.

Immunocytochemistry

For immunostaining, primary neuronal cultures were grown on 13-mm coverslips (Marienfeld) in 24-well plates. At the appropriate times, cultures were fixed with fresh 4% (wt/vol) paraformaldehyde (Sigma-Aldrich) for 10 min, and the cells permeabilized by treatment with 0.3% Triton X-100 in PBS for 10 min. After blocking with 5% (wt/vol) BSA in PBS for 1 h, primary antibodies were added and incubated overnight at 4°C. The following day, coverslips were washed three times (10 min each) with PBS. After rinsing, secondary antibodies were applied for 1 h at room temperature, followed by three additional washes with PBS. The coverslips were then inverted and mounted on glass slides with ProLong Gold Antifade Reagent (Life Technologies). Immunofluorescence was analyzed and Z-stack maximum projected images were photographed using a Leica TCS SP8 confocal laser scanning platform equipped with Leica HyD hybrid detector and visualized through a HC PL APO CS2 63× (1.40 NA) oil-immersion objective. Image acquisition was controlled by the LAS X.

For immunostaining of brain sections, we performed antigen retrieval by treating the mounted cryostat sections with citrate buffer at 95°C for 15 min, followed by cooling to room temperature for 1 h. Sections were rinsed in PBS, blocked with 5% (vol/vol) donkey serum/PBS for 1 h before immunostaining as above.

LIVE/DEAD cell viability assays

The LIVE/DEAD viability/cytotoxicity kit for mammalian cells was purchased from Thermo Fisher. The method relies on two probes: calcein AM and ethidium homodimer-1 (EthD-1). Cultured cortical neurons or human fibroblasts were washed three times with 500 volumes of Dulbecco's PBS (D-PBS) to remove or dilute serum esterase activity generally present in serum-supplemented growth media. Two hundred microliters of the calcein/EthD-1 working solution (1 µM and 2 µM, respectively in D-PBS) were applied to the surface of a coverslip or 35-mm disposable Petri dish and incubated for 45 min at room temperature in the dark. Imaging was performed on a Leica TCS SP8 confocal laser scanning platform, equipped with Leica HyD hybrid detector and visualized through a HC PL APO CS2 63× (1.40) NA oil-immersion objective. Image acquisition was controlled by the LAS X, with the sequential scanning program. Calcein was excited at 485 ± 15 nm, and emission was measured at 530 ± 15 nm; EthD-1 was excited at 530 ± 15 nm with emission measured at 645 ± 15 nm. Quantification of live (green) and dead (red) cells was performed randomly on 10 fields from each of three to four blinded samples. The percentage of dead cells was calculated as (number of dead cells/total number of live and dead cells) × 100%.

Monitoring NRF1 nuclear transcription activity and changes in mitochondrial morphology

The NRF1mitoGFP reporter was a gift from K.J. Tronstad (University of Bergen, Bergen, Norway; Hodneland Nilsson et al., 2015). Cortical neurons were transfected with reporter-expressing plasmids on DIV 9. 24 h after transfection, cells were exposed to one of the following drug conditions: (1) vehicle (saline); (2) 1 µM atractyloside alone; or (3) atractyloside plus 5 mM NAC (Chao et al., 2016), followed by live-imaging for another 24 h in a 95% air/5% CO_2–gassed chamber mounted on a Leica TCS SP8 confocal laser scanning platform, equipped with Leica HyD hybrid detector and visualized through a HC PL APO CS2 63× (1.40 NA) oil-immersion objective. Image acquisition was controlled by LAS X. GFP was excited at 480 ± 15 nm and emission detected at 520 ± 15 nm. To analyze mitochondrial morphology the GFP signals of each cell (in a different set of cultures) were imaged at 24 h after drug treatment, and later, the Z-stack images were used to construct the 3D model by the LAS X for morphology analysis.

Nrf1 expression plasmid and mutated Nrf1

A mouse cDNA ORF clone encoding NM_001164226, tagged with Myc-FLAG at the C-terminus, was purchased from OriGene (MR226726). EGFP or mCherry coding sequences were fused to the C-terminus, replacing the Myc-FLAG tag, by Gibson assembly to make pCMV6-Nrf1-EGFP. Site-directed mutagenesis used the NEBaseChanger kit (NEB), with oligonucleotide primers designed using the manufacturer's website. All mutations and deletions were confirmed by sequencing.

Quantification of the relative abundance of mouse mitochondrial DNA to nuclear DNA

The quantification protocol for mouse mitochondrial DNA without coamplification of nuclear mitochondrial insertion sequences was adopted (Malik et al., 2016). To prepare genomic DNA, mouse tissue samples were homogenized using TissueLyser (Qiagen) to eliminate cross-contamination. Total genomic DNA was extracted using the DNeasy Blood and Tissue kit according to the manufacturer's instruction (Qiagen). Before proceeding to qPCR, the DNA template was subjected to pretreatment shearing (Bath sonicator Kerry, Pulsatron 55: 38 kHz for 10 min), as described previously to avoid dilution bias (Malik et al., 2011). The template concentration was determined using NanoDrop and adjusted to 10 ng/µl. To avoid errors arising from repeated freeze–thaw cycles, DNA samples were kept at 4°C for the duration of study.

The mitochondrial DNA content was assessed by absolute quantification using real-time PCR. Primers of mouse mitochondrial DNA (mMito) and mouse single copy nuclear β-2 microglobulin were used to amplify the respective products. PCR products were purified and used to prepare dilution standards for both amplicons using a range of dilutions from 10^2–10^8 copies per 2 µl for quantification. Mitochondrial copy number per cell was determined by carrying out qPCR in a total volume of 10 µl, containing 5 µl of Quantifast SYBR Master Mix (Qiagen), 0.5 µl of forward and reverse primer (400 nM final concentration each), 2 µl template DNA, and 2 µl DNase-free water. The reactions were performed in a Roche LightCycler 480 instrument using the following protocol: preincubation at 95°C for 5 min (1 cycle); denaturation at 95°C for 10 s; annealing and extension at 60°C for 30 s (40 cycles); melting at 95°C for 5 s, 65°C for 60 s, and 95°C continues (1 cycle); and cooling at 40°C for 30 s. The specificity of the primers was confirmed by the presence of a single melt peak. qPCR efficiency calculated from the slope between 95 and 105%, with coefficient of reaction R^2 = 0.98–0.99. A total of seven to nine biological replicates by four technical replicates were performed for each treatment group. Data were analyzed using the ΔΔCt method.

Statistical analysis

Data are presented as mean ± SEM. Data distribution was assumed to be normal, but this was not formally tested. Statistical significance was analyzed using one-way ANOVA, two-way ANOVA, or two-sided Student's *t* test as indicated in each figure legend.

Online supplemental material

Fig. S1 shows impaired expression of OXPHOS genes in human A-T cerebellum. Fig. S2 shows loss of ATM impairs mitochondrial usage of pyruvate, but enhanced lactate production in mouse neurons. Fig. S3 shows loss of ATM impairs ATP insufficiency response of human fibroblasts. Fig. S4 shows chronic insufficient ATP induces oxidative stress, activation of NRF1, and mitochondrial biogenesis. Fig. S5 shows Western blot analysis of NRF1 phosphorylation, homodimerization, and nuclear localization, demonstrating the requirement of T259 for ATM activation induced by oxidative stress. Table S1 shows raw data of multiple bioinformatics analyses. Information regarding to reagents and resources, including the sources of antibodies, chemicals and assay kits, recombinant DNA, sequences of primers for both real-time PCR and site-directed mutagenesis, and a list of software and algorithms used in this study is included in Table S2.

Acknowledgments

We acknowledge the staff at the University Research Facility in Life Science of Hong Kong Polytechnic University for their technical support in experiments.

This work was financially supported by Research Grants Council, Hong Kong Special Administrative Region (grants GRF660813, GRF16103317, and GRF16100718), an RGC/Hong Kong University of Science and Technology (HKUST) initiation grant (IGN16SC02), and HKUST Institute for Advanced Study Junior Fellowship and Alzheimer's Association Research Fellowship (grant AARF-17-531566) to H.-M. Chow. M.R. Swerdel and R.P. Hart were supported by National Institutes of Health grant R01 ES026057.

The authors declare no competing financial interests.

Author contributions: H.-M. Chow designed the experiments, performed the work, analyzed the data, and wrote the manuscript. A. Cheng, X. Song, and M.R. Swerdel performed essential work, helped in the analysis of the data, and helped in the writing of the experiments. R.P. Hart and K. Herrup designed experiments, analyzed data, and wrote the manuscript.

Submitted: 28 June 2018
Revised: 27 October 2018
Accepted: 26 December 2018

References

Abramov, A.Y., T.K. Smulders-Srinivasan, D.M. Kirby, R. Acin-Perez, J.A. Enriquez, R.N. Lightowlers, M.R. Duchen, and D.M. Turnbull. 2010. Mechanism of neurodegeneration of neurons with mitochondrial DNA mutations. *Brain.* 133:797–807. https://doi.org/10.1093/brain/awq015

Aird, K.M., A.J. Worth, N.W. Snyder, J.V. Lee, S. Sivanand, Q. Liu, I.A. Blair, K.E. Wellen, and R. Zhang. 2015. ATM couples replication stress and metabolic reprogramming during cellular senescence. *Cell Reports.* 11:893–901. https://doi.org/10.1016/j.celrep.2015.04.014

Ashley, C.N., K.D. Hoang, D.R. Lynch, S.L. Perlman, and B.L. Maria. 2012. Childhood ataxia: clinical features, pathogenesis, key unanswered questions, and future directions. *J. Child Neurol.* 27:1095–1120. https://doi.org/10.1177/0883073812448840

Bargiela, D., P. Shanmugarajah, C. Lo, E.L. Blakely, R.W. Taylor, R. Horvath, S. Wharton, P.F. Chinnery, and M. Hadjivassiliou. 2015. Mitochondrial pathology in progressive cerebellar ataxia. *Cerebellum Ataxias.* 2:16. https://doi.org/10.1186/s40673-015-0035-x

Calvo, S.E., K.R. Clauser, and V.K. Mootha. 2016. MitoCarta2.0: an updated inventory of mammalian mitochondrial proteins. *Nucleic Acids Res.* 44(D1):D1251–D1257. https://doi.org/10.1093/nar/gkv1003

Carter, B.C., and B.P. Bean. 2009. Sodium entry during action potentials of mammalian neurons: incomplete inactivation and reduced metabolic efficiency in fast-spiking neurons. *Neuron.* 64:898–909. https://doi.org/10.1016/j.neuron.2009.12.011

Chang, J.T., and J.R. Nevins. 2006. GATHER: a systems approach to interpreting genomic signatures. *Bioinformatics.* 22:2926–2933. https://doi.org/10.1093/bioinformatics/btl483

Chao, M.W., C.P. Chen, Y.H. Yang, Y.C. Chuang, T.Y. Chu, and C.Y. Tseng. 2016. N-acetylcysteine attenuates lipopolysaccharide-induced impairment in lamination of Ctip2-and Tbr1- expressing cortical neurons in the developing rat fetal brain. *Sci. Rep.* 6:32373. https://doi.org/10.1038/srep32373

Chen, W., and M. Guéron. 1992. The inhibition of bovine heart hexokinase by 2-deoxy-D-glucose-6-phosphate: characterization by 31P NMR and metabolic implications. *Biochimie.* 74:867–873. https://doi.org/10.1016/0300-9084(92)90070-U

Chen, J., Y. Chen, G. Vail, H. Chow, Y. Zhang, L. Louie, J. Li, R.P. Hart, M.R. Plummer, and K. Herrup. 2016a. The impact of glutamine supplementation on the symptoms of ataxia-telangiectasia: a preclinical assessment. *Mol. Neurodegener.* 11:60. https://doi.org/10.1186/s13024-016-0127-y

Chen, W.W., E. Freinkman, T. Wang, K. Birsoy, and D.M. Sabatini. 2016b. Absolute Quantification of Matrix Metabolites Reveals the Dynamics of Mitochondrial Metabolism. *Cell.* 166:1324–1337.e11. https://doi.org/10.1016/j.cell.2016.07.040

Chen, Y., H.G. Shertzer, S.N. Schneider, D.W. Nebert, and T.P. Dalton. 2005. Glutamate cysteine ligase catalysis: dependence on ATP and modifier subunit for regulation of tissue glutathione levels. *J. Biol. Chem.* 280:33766–33774. https://doi.org/10.1074/jbc.M504604200

Choi, H.B., G.R. Gordon, N. Zhou, C. Tai, R.L. Rungta, J. Martinez, T.A. Milner, J.K. Ryu, J.G. McLarnon, M. Tresguerres, et al. 2012. Metabolic communication between astrocytes and neurons via bicarbonate-responsive soluble adenylyl cyclase. *Neuron.* 75:1094–1104. https://doi.org/10.1016/j.neuron.2012.08.032

Chow, H.M., D. Guo, J.C. Zhou, G.Y. Zhang, H.F. Li, K. Herrup, and J. Zhang. 2014. CDK5 activator protein p25 preferentially binds and activates GSK3β. *Proc. Natl. Acad. Sci. USA.* 111:E4887–E4895. https://doi.org/10.1073/pnas.1402627111

Cribbs, A.P., A. Kennedy, B. Gregory, and F.M. Brennan. 2013. Simplified production and concentration of lentiviral vectors to achieve high transduction in primary human T cells. *BMC Biotechnol.* 13:98. https://doi.org/10.1186/1472-6750-13-98

DiMauro, S., and P. Rustin. 2009. A critical approach to the therapy of mitochondrial respiratory chain and oxidative phosphorylation diseases. *Biochim. Biophys. Acta.* 1792:1159–1167. https://doi.org/10.1016/j.bbadis.2008.10.015

Evans, M.J., and R.C. Scarpulla. 1990. NRF-1: a trans-activator of nuclear-encoded respiratory genes in animal cells. *Genes Dev.* 4:1023–1034. https://doi.org/10.1101/gad.4.6.1023

Fang, E.F., M. Scheibye-Knudsen, L.E. Brace, H. Kassahun, T. SenGupta, H. Nilsen, J.R. Mitchell, D.L. Croteau, and V.A. Bohr. 2014. Defective mitophagy in XPA via PARP-1 hyperactivation and NAD(+)/SIRT1 reduction. *Cell.* 157:882–896. https://doi.org/10.1016/j.cell.2014.03.026

Fang, E.F., H. Kassahun, D.L. Croteau, M. Scheibye-Knudsen, K. Marosi, H. Lu, R.A. Shamanna, S. Kalyanasundaram, R.C. Bollineni, M.A. Wilson, et al. 2016. NAD^+ Replenishment Improves Lifespan and Healthspan in Ataxia Telangiectasia Models via Mitophagy and DNA Repair. *Cell Metab.* 24:566–581. https://doi.org/10.1016/j.cmet.2016.09.004

Garcia-Gutierrez, P., M. Mundi, and M. Garcia-Dominguez. 2012. Association of bromodomain BET proteins with chromatin requires dimerization through the conserved motif B. *J. Cell Sci.* 125:3671–3680. https://doi.org/10.1242/jcs.105841

Gugneja, S., and R.C. Scarpulla. 1997. Serine phosphorylation within a concise amino-terminal domain in nuclear respiratory factor 1 enhances DNA binding. *J. Biol. Chem.* 272:18732–18739. https://doi.org/10.1074/jbc.272.30.18732

Guo, Z., S. Kozlov, M.F. Lavin, M.D. Person, and T.T. Paull. 2010. ATM activation by oxidative stress. *Science.* 330:517–521. https://doi.org/10.1126/science.1192912

Hall, C.N., M.C. Klein-Flügge, C. Howarth, and D. Attwell. 2012. Oxidative phosphorylation, not glycolysis, powers presynaptic and postsynaptic mechanisms underlying brain information processing. *J. Neurosci.* 32:8940–8951. https://doi.org/10.1523/JNEUROSCI.0026-12.2012

Hanson, G.T., R. Aggeler, D. Oglesbee, M. Cannon, R.A. Capaldi, R.Y. Tsien, and S.J. Remington. 2004. Investigating mitochondrial redox potential with redox-sensitive green fluorescent protein indicators. *J. Biol. Chem.* 279:13044–13053. https://doi.org/10.1074/jbc.M312846200

Hargreaves, I.P., Y. Sheena, J.M. Land, and S.J. Heales. 2005. Glutathione deficiency in patients with mitochondrial disease: implications for pathogenesis and treatment. *J. Inherit. Metab. Dis.* 28:81–88. https://doi.org/10.1007/s10545-005-4160-1

Hildyard, J.C., C. Ammälä, I.D. Dukes, S.A. Thomson, and A.P. Halestrap. 2005. Identification and characterisation of a new class of highly specific and potent inhibitors of the mitochondrial pyruvate carrier. *Biochim. Biophys. Acta.* 1707:221–230. https://doi.org/10.1016/j.bbabio.2004.12.005

Hodneland Nilsson, L.I., I.K. Nitschke Pettersen, J. Nikolaisen, D. Micklem, H. Avsnes Dale, G. Vatne Røsland, J. Lorens, and K.J. Tronstad. 2015. A new live-cell reporter strategy to simultaneously monitor mitochondrial biogenesis and morphology. *Sci. Rep.* 5:17217. https://doi.org/10.1038/srep17217

Hornbeck, P.V., B. Zhang, B. Murray, J.M. Kornhauser, V. Latham, and E. Skrzypek. 2015. PhosphoSitePlus, 2014: mutations, PTMs and recalibrations. *Nucleic Acids Res.* 43(D1):D512–D520. https://doi.org/10.1093/nar/gku1267

Howarth, C., C.M. Peppiatt-Wildman, and D. Attwell. 2010. The energy use associated with neural computation in the cerebellum. *J. Cereb. Blood Flow Metab.* 30:403–414. https://doi.org/10.1038/jcbfm.2009.231

Howarth, C., P. Gleeson, and D. Attwell. 2012. Updated energy budgets for neural computation in the neocortex and cerebellum. *J. Cereb. Blood Flow Metab.* 32:1222–1232. https://doi.org/10.1038/jcbfm.2012.35

Huang da, W., B.T. Sherman, and R.A. Lempicki. 2009. Systematic and integrative analysis of large gene lists using DAVID bioinformatics resources. *Nat. Protoc.* 4:44–57. https://doi.org/10.1038/nprot.2008.211

Jiang, D., Y. Zhang, R.P. Hart, J. Chen, K. Herrup, and J. Li. 2015. Alteration in 5-hydroxymethylcytosine-mediated epigenetic regulation leads to Purkinje cell vulnerability in ATM deficiency. *Brain.* 138:3520–3536. https://doi.org/10.1093/brain/awv284

Joshi, D.C., and J.C. Bakowska. 2011. Determination of mitochondrial membrane potential and reactive oxygen species in live rat cortical neurons. *J. Vis. Exp.* (51):2704.

Jourdain, P., I. Allaman, K. Rothenfusser, H. Fiumelli, P. Marquet, and P.J. Magistretti. 2016. L-Lactate protects neurons against excitotoxicity: implication of an ATP-mediated signaling cascade. *Sci. Rep.* 6:21250. https://doi.org/10.1038/srep21250

Kastan, M.B., and D.S. Lim. 2000. The many substrates and functions of ATM. *Nat. Rev. Mol. Cell Biol.* 1:179–186. https://doi.org/10.1038/35043058

Kelley, L.A., S. Mezulis, C.M. Yates, M.N. Wass, and M.J. Sternberg. 2015. The Phyre2 web portal for protein modeling, prediction and analysis. *Nat. Protoc.* 10:845–858. https://doi.org/10.1038/nprot.2015.053

Kobayashi, A., T. Tsukide, T. Miyasaka, T. Morita, T. Mizoroki, Y. Saito, Y. Ihara, A. Takashima, N. Noguchi, A. Fukamizu, et al. 2011. Central nervous system-specific deletion of transcription factor Nrf1 causes progressive motor neuronal dysfunction. *Genes Cells.* 16:692–703. https://doi.org/10.1111/j.1365-2443.2011.01522.x

Koopman, W.J., F. Distelmaier, J.A. Smeitink, and P.H. Willems. 2013. OXPHOS mutations and neurodegeneration. *EMBO J.* 32:9–29. https://doi.org/10.1038/emboj.2012.300

Lax, N.Z., P.D. Hepplewhite, A.K. Reeve, V. Nesbitt, R. McFarland, E. Jaros, R.W. Taylor, and D.M. Turnbull. 2012. Cerebellar ataxia in patients with mitochondrial DNA disease: a molecular clinicopathological study. *J. Neuropathol. Exp. Neurol.* 71:148–161. https://doi.org/10.1097/NEN.0b013e318244477d

Le Masson, G., S. Przedborski, and L.F. Abbott. 2014. A computational model of motor neuron degeneration. *Neuron.* 83:975–988. https://doi.org/10.1016/j.neuron.2014.07.001

Li, J., R.P. Hart, E.M. Mallimo, M.R. Swerdel, A.W. Kusnecov, and K. Herrup. 2013. EZH2-mediated H3K27 trimethylation mediates neurodegeneration in ataxia-telangiectasia. *Nat. Neurosci.* 16:1745–1753. https://doi.org/10.1038/nn.3564

Malik, A.N., R. Shahni, A. Rodriguez-de-Ledesma, A. Laftah, and P. Cunningham. 2011. Mitochondrial DNA as a non-invasive biomarker: accurate quantification using real time quantitative PCR without co-amplification of pseudogenes and dilution bias. *Biochem. Biophys. Res. Commun.* 412:1–7. https://doi.org/10.1016/j.bbrc.2011.06.067

Malik, A.N., A. Czajka, and P. Cunningham. 2016. Accurate quantification of mouse mitochondrial DNA without co-amplification of nuclear mitochondrial insertion sequences. *Mitochondrion.* 29:59–64. https://doi.org/10.1016/j.mito.2016.05.003

McCommis, K.S., and B.N. Finck. 2015. Mitochondrial pyruvate transport: a historical perspective and future research directions. *Biochem. J.* 466:443–454. https://doi.org/10.1042/BJ20141171

McKenzie, M., D. Liolitsa, N. Akinshina, M. Campanella, S. Sisodiya, I. Hargreaves, N. Nirmalananthan, M.G. Sweeney, P.M. Abou-Sleiman, N.W. Wood, et al. 2007. Mitochondrial ND5 gene variation associated with encephalomyopathy and mitochondrial ATP consumption. *J. Biol. Chem.* 282:36845–36852. https://doi.org/10.1074/jbc.M704158200

Morita, A., K. Tanimoto, T. Murakami, T. Morinaga, and Y. Hosoi. 2014. Mitochondria are required for ATM activation by extranuclear oxidative stress in cultured human hepatoblastoma cell line Hep G2 cells. *Biochem. Biophys. Res. Commun.* 443:1286–1290. https://doi.org/10.1016/j.bbrc.2013.12.139

Nicholls, D.G., V.M. Darley-Usmar, M. Wu, P.B. Jensen, G.W. Rogers, and D.A. Ferrick. 2010. Bioenergetic profile experiment using C2C12 myoblast cells. *J. Vis. Exp.* (46):2511.

Novoa, W.B., A.D. Winer, A.J. Glaid, and G.W. Schwert. 1959. Lactic dehydrogenase. V. Inhibition by oxamate and by oxalate. *J. Biol. Chem.* 234:1143–1148.

Pierce, B.G., K. Wiehe, H. Hwang, B.H. Kim, T. Vreven, and Z. Weng. 2014. ZDOCK server: interactive docking prediction of protein-protein complexes and symmetric multimers. *Bioinformatics.* 30:1771–1773. https://doi.org/10.1093/bioinformatics/btu097

San Martín, A., S. Ceballo, F. Baeza-Lehnert, R. Lerchundi, R. Valdebenito, Y. Contreras-Baeza, K. Alegría, and L.F. Barros. 2014. Imaging mitochondrial flux in single cells with a FRET sensor for pyruvate. *PLoS One.* 9:e85780. https://doi.org/10.1371/journal.pone.0085780

Saraiva, L.M., G.S. Seixas da Silva, A. Galina, W.S. da-Silva, W.L. Klein, S.T. Ferreira, and F.G. De Felice. 2010. Amyloid-β triggers the release of neuronal hexokinase 1 from mitochondria. *PLoS One.* 5:e15230. https://doi.org/10.1371/journal.pone.0015230

Satoh, J., N. Kawana, and Y. Yamamoto. 2013. Pathway Analysis of ChIP-Seq-Based NRF1 Target Genes Suggests a Logical Hypothesis of their Involvement in the Pathogenesis of Neurodegenerative Diseases. *Gene Regul. Syst. Bio.* 7:139–152.

Scarpulla, R.C. 2008. Transcriptional paradigms in mammalian mitochondrial biogenesis and function. *Physiol. Rev.* 88:611–638. https://doi.org/10.1152/physrev.00025.2007

Scheibye-Knudsen, M., K. Scheibye-Alsing, C. Canugovi, D.L. Croteau, and V.A. Bohr. 2013. A novel diagnostic tool reveals mitochondrial pathology in human diseases and aging. *Aging (Albany N.Y.).* 5:192–208.

Schütt, F., S. Aretz, G.U. Auffarth, and J. Kopitz. 2012. Moderately reduced ATP levels promote oxidative stress and debilitate autophagic and phagocytic capacities in human RPE cells. *Invest. Ophthalmol. Vis. Sci.* 53:5354–5361. https://doi.org/10.1167/iovs.12-9845

Subramanian, A., P. Tamayo, V.K. Mootha, S. Mukherjee, B.L. Ebert, M.A. Gillette, A. Paulovich, S.L. Pomeroy, T.R. Golub, E.S. Lander, and J.P. Mesirov. 2005. Gene set enrichment analysis: a knowledge-based approach for interpreting genome-wide expression profiles. *Proc. Natl. Acad. Sci. USA.* 102:15545–15550. https://doi.org/10.1073/pnas.0506580102

Sugimori, M., and R.R. Llinás. 1990. Real-time imaging of calcium influx in mammalian cerebellar Purkinje cells in vitro. *Proc. Natl. Acad. Sci. USA.* 87:5084–5088. https://doi.org/10.1073/pnas.87.13.5084

Tantama, M., J.R. Martínez-François, R. Mongeon, and G. Yellen. 2013. Imaging energy status in live cells with a fluorescent biosensor of the intracellular ATP-to-ADP ratio. *Nat. Commun.* 4:2550. https://doi.org/10.1038/ncomms3550

Valentin-Vega, Y.A., K.H. Maclean, J. Tait-Mulder, S. Milasta, M. Steeves, F.C. Dorsey, J.L. Cleveland, D.R. Green, and M.B. Kastan. 2012. Mitochondrial dysfunction in ataxia-telangiectasia. *Blood.* 119:1490–1500. https://doi.org/10.1182/blood-2011-08-373639

Wang, Z.J., C.L. Liang, G.M. Li, C.Y. Yu, and M. Yin. 2007. Stearic acid protects primary cultured cortical neurons against oxidative stress. *Acta Pharmacol. Sin.* 28:315–326. https://doi.org/10.1111/j.1745-7254.2007.00512.x

Watters, D.J. 2003. Oxidative stress in ataxia telangiectasia. *Redox Rep.* 8:23–29. https://doi.org/10.1179/135100003125001206

Waypa, G.B., J.D. Marks, R. Guzy, P.T. Mungai, J. Schriewer, D. Dokic, and P.T. Schumacker. 2010. Hypoxia triggers subcellular compartmental redox signaling in vascular smooth muscle cells. *Circ. Res.* 106:526–535. https://doi.org/10.1161/CIRCRESAHA.109.206334

Welsh, J.P., G. Yuen, D.G. Placantonakis, T.Q. Vu, F. Haiss, E. O'Hearn, M.E. Molliver, and S.A. Aicher. 2002. Why do Purkinje cells die so easily after global brain ischemia? Aldolase C, EAAT4, and the cerebellar contribution to posthypoxic myoclonus. *Adv. Neurol.* 89:331–359.

Xu, Y., T. Ashley, E.E. Brainerd, R.T. Bronson, M.S. Meyn, and D. Baltimore. 1996. Targeted disruption of ATM leads to growth retardation, chromosomal fragmentation during meiosis, immune defects, and thymic lymphoma. *Genes Dev.* 10:2411–2422. https://doi.org/10.1101/gad.10.19.2411

Yan, Y., C.L. Wei, W.R. Zhang, H.P. Cheng, and J. Liu. 2006. Cross-talk between calcium and reactive oxygen species signaling. *Acta Pharmacol. Sin.* 27:821–826. https://doi.org/10.1111/j.1745-7254.2006.00390.x

Zakikhani, M., M. Bazile, S. Hashemi, S. Javeshghani, D. Avizonis, J. St Pierre, and M.N. Pollak. 2012. Alterations in cellular energy metabolism associated with the antiproliferative effects of the ATM inhibitor KU-55933 and with metformin. *PLoS One.* 7:e49513. https://doi.org/10.1371/journal.pone.0049513

Zambelli, F., G. Pesole, and G. Pavesi. 2009. Pscan: finding over-represented transcription factor binding site motifs in sequences from co-regulated or co-expressed genes. *Nucleic Acids Res.* 37(suppl_2):W247–W252. https://doi.org/10.1093/nar/gkp464